The $\mu \to e\gamma$ Experiment – Goals and Status

A. Baldini[4*], A. de Bari[5], L. M. Barkov[1], C. Bemporad[4], P. Cattaneo[5], G. Cecchet[5], F. Cei[4], T. Doke[8], J. Egger[6], M. Grassi[4], A. A. Grebenuk[1], T. Haruyama[2], P.-R. Kettle[6], B. Khazin[1], J. Kikuchi[8], Y. Kuno[3], A. Maki[2], Y. Makida[2], T. Mashimo[7], S. Mihara[7], T. Mitsuhashi[7], T. Mori[7*], D. Nicolò[4], H. Nishiguchi[7], H. Okada[8], W. Ootani[7], K. Ozone[7], R. Pazzi[4], S. Ritt[6], T. Saeki[7], R. Sawada[7], F. Sergiampietri[4], G. Signorelli[4], V. P. Smakhtin[1], S. Suzuki[8], K. Terasawa[8], A. Yamamoto[2], M. Yamashita[8], S. Yamashita[7], K. Yoshimura[2], T. Yoshimura[8]

(Collaboration for the $\mu \to e\gamma$ Experiment at PSI)

[1]BINP, Novosibirsk, Russia
[2]KEK, Tsukuba, Japan
[3]Osaka University, Osaka, Japan
[4]University of Pisa and INFN, Pisa, Italy
[5]INFN, Pavia, Italy
[6]PSI, Villigen, Switzerland
[7]University of Tokyo, Tokyo, Japan
[8]Waseda University, Tokyo, Japan

July 2002

Abstract

This note describes the goals and the updated status of the $\mu \to e\gamma$ experiment, as of July 1st, 2002. Many items are still left open: It will be updated periodically and when any major development occurs.

---

[*]spokesperson

1 Overall Goals of the Experiment

1.1 Sensitivity

The aim is to reach a branching ratio sensitivity well below the current limit (1.2×10^{-11}) to probe the supersymmetric grand unification and the new physics underlying the neutrino oscillations.

- Proposal[1]: 0.5 background events for 10^{14} accepted muon decays (a single event sensitivity of 1×10^{-14}), corresponding to a 90% C.L. upper bound of 2.9×10^{-14} if only background events.

- Present: to be re-evaluated with updated detector resolutions and acceptances; Full MC simulations must be made.
  A crude estimate based on conservative extrapolation of the presently available knowledge of the detector performance indicates that the experiment should be able to achieve at least the following sensitivity: 0.6 background events for $(2–3)\times10^{13}$ accepted muon decays (a single event sensitivity of $(4–6)\times10^{-14}$), corresponding to a 90% C.L. upper bound of $(1.0–1.6)\times10^{-13}$ if only background events.

1.2 Schedule

Results should be obtained before the LHC experiments (and the proposed $\mu \rightarrow$ e conversion experiment [3]) to make a possible first discovery or place most stringent limits on the new physics.

- Proposal: Engineering runs in 2003; A total running time is 50 "PSI beam weeks" (1 PSI beam weeks = 4×10^5 sec).

- present: Beam line tuning with the COBRA magnet in later part of 2003; Engineering runs in 2004. Possibly need more running time to achieve optimal performance.

2 Expected Performance

2.1 Accidental Background Rate B_{acc}

The experimental reach will be limited by the accidental background, which may be roughly evaluated from the detector resolutions by the following formula (see Appendix A of [1] and Chapter X of [2]):

$$B_{acc} = AR_\mu(\delta\theta_{\mathrm{e}\gamma})^2(\delta p_{\mathrm{e}})(\delta E_\gamma)^2(\delta t_{\mathrm{e}\gamma})$$

where R_μ is the muon stopping rate. An accurate evaluation of the background rate requires full MC simulation taking into account the effects of pile-up, correlations between the detector responses, etc. The value of A may be obtained from the proposal where a full simulation was employed to evaluate B_{acc}.

2.2 Expected Sensitivity S_{90}

Assuming no signal event, the expected upper limit on the $\mu \to \mathrm{e}\gamma$ branching ratio at 90% C.L. is given by

$$S_{90} = \frac{N_{90}}{R_\mu T(\Omega/4\pi)\epsilon_{\mathrm{e}}\epsilon_\gamma\epsilon_{sel}}$$

while the single event sensitivity S_{1ev} is defined by replacing N_{90} with 1 in the numerator. Here T is the total running time, Ω the geometrical acceptance, ϵ the detection and selection efficiencies. N_{90} is the 90% upper limit on the number of $\mu \to \mathrm{e}\gamma$ events corresponding to the expected background $N_{acc} = R_\mu T B_{acc}$. The sensitivity S_{90} roughly scales as

$$S_{90} \propto \frac{R_\mu(\delta\theta_{\mathrm{e}\gamma})^2(\delta p_{\mathrm{e}})(\delta E_\gamma)^2(\delta t_{\mathrm{e}\gamma})}{(\Omega/4\pi)\epsilon_{\mathrm{e}}\epsilon_\gamma\epsilon_{sel}}.$$

The sensitivity improves for a lower muon rate, but it would then require longer running time to reach that sensitivity.

2.3 Estimate of Performance

The background and sensitivity as estimated in the proposal are shown in Table 1 together with the expected detector resolutions and efficiencies.

The table also contains a quite conservative evaluation of the sensitivity using the presently available knowledge of the detector performance. For the photon detector, a 100 cm absorption length of scintillation light, already available with the current level of xenon purity in the prototype detector, is assumed, and no elaborate optimization of detector configuration has been made. The change in the photon detection efficiency reflects the recent update of the front material effects. See the corresponding sections for more details on the expected detector performance. The evaluated sensitivity, which is considered to be the worst we could attain, is 17–28 times worse than that of the proposal with a 29 % poorer acceptance, but it already reaches a single event sensitivity of (3.8–5.6)$\times 10^{-14}$ with 0.6 expected background events.

Here the timing resolution for eγ coincidence, $\delta t_{\mathrm{e}\gamma}$, is derived from the timing resolutions for each particle, δt_{e} and δt_γ, and the position resolution for photon conversion δz_γ. The opening angle resolution $\delta\theta_{e\gamma}$ is based on the photon position resolution δx_γ at the photon detector (≈ 65 cm from the stopping target), the positron angle resolution $\delta\theta_e$, and the position resolution for the muon decay point at the target δd_e.

This table will be updated as new results from the detector prototype tests and the MC simulation studies will become available.

Table 1: Background and sensitivity with all the relevant parameters. Resolutions are given in FWHM. The numbers in the parentheses indicate slightly degraded resolutions in part of the detector acceptance. The minimum expected performance based on the conservative extrapolation of the present knowledge is also shown.

	proposal	
δE_γ (%)	1.4 (2.0)	**4.0–4.5**
δp_e (%)	0.7	**0.7–0.9**
$\delta t_{e\gamma}$ (nsec)	0.15	0.15
$\cdot\ \delta t_e$ (nsec)	0.1	0.1
$\cdot\ \delta t_\gamma$ (nsec)	0.1	0.1
$\cdot\ \delta z_\gamma$ (mm)	16	**16–18**
$\delta\theta_{e\gamma}$ (mrad)	12 (14)	**17–20.5**
$\cdot\ \delta\theta_e$ (mrad)	9	**9–12**
$\cdot\ \delta d_e$ (mm)	2.1	**2.1–2.5**
$\cdot\ \delta x_\gamma$ (mm)	4 (7)	**9–10.5**
$\Omega/4\pi$	0.09	0.09
ϵ_e	0.95	**0.9**
ϵ_γ	0.7	**0.6**
ϵ_{sel}	0.8	**0.7**
R_μ /sec	1.0×10^8	$\mathbf{(0.2–0.3) \times 10^8}$
T sec	2×10^7	$\mathbf{2.6 \times 10^7}$
S_{1ev}	0.94×10^{-14}	(3.8–5.6)$\times 10^{-14}$
B_{acc}	0.5×10^{-14}	(2.2–3.5)$\times 10^{-14}$
N_{acc}	0.5	0.6
S_{90}	2.9×10^{-14}	(1.0–1.6)$\times 10^{-13}$

3 Collaboration

In anticipation of stronger involvement of the Italian group in this experiment, with more Italian institutes to participate, the collaboration has been slightly re-organized: spokespersonship to be shared by T. Mori and A. Baldini, together with S. Ritt as technical coordinator. The responsibilities for the detectors are now more evenly shared by the Japanese, the Italian, and the Swiss groups, which will be also reflected in our plan for budget subdivision to be presented at the committee meeting in July:

- spokespersons: T. Mori, A. Baldini
- technical coordinator: S. Ritt
- responsible institutes and contact persons:
  - Beam Line: PSI (P.-R. Kettle)
  - COBRA Magnet: KEK–Tokyo (W. Ootani)
  - Drift Chamber: PSI (J. Egger)
  - Timing Counter: Pisa (A. Baldini)
  - Photon Detector: Tokyo–KEK–Pisa (S. Mihara)
  - Trigger: Pisa (M. Grassi)
  - Electronics and DAQ: PSI (S. Ritt)

All the collaborators are listed on the first page of this report. The collaborators from Waseda University, BINP and Osaka University mostly help with the technical aspects of the photon detector.

We feel that we are somewhat short of manpower in the software area of the Drift Chamber and possibly also in the Beam Line. We therefore request the PSI management that more manpower be made available in these areas possibly by hiring a few posdocs. Graduate students from the other institutes could also help, but it would require PSI to financially support their stay at PSI.

4 πE5 Beam Studies:

In order to achieve the design goals of the detectors involved in the experiment [1], it is also necessary to have a well understood beam transport system deliver a high intensity surface muon beam, which is capable of being stopped in a thin target, with a minimum of contaminant particles entering the detectors. Two basic methods are applicable to achieve a minimum of beam positron contamination from being transfered, from the production target, to the detector, and have an optimal muon stopping rate in the experiment. Either, a combined solution can be used, involving degrading the beam momentum, so that the residual range matches the target thickness, as well as introducing an energy-loss difference to the positrons and muons, enabling a separation in the following magnetic elements. Or, the beam positron contamination can be significantly reduced using crossed electrostatic and magnetic fields , i.e. Wien-filter, as a mass selection device, with either a reduced initial beam momentum and a thin stopping target, or the nominal momentum and a separate degrader.

Since the πE5 beamline is the most intense source of surface muons, the choice was clear. However, with two separate branches of the beamline, a "U"-branch feeding the πE52-area and a "Z"-branch feeding the πE51-area c.f. Figure 1, a optimal choice has to be made.

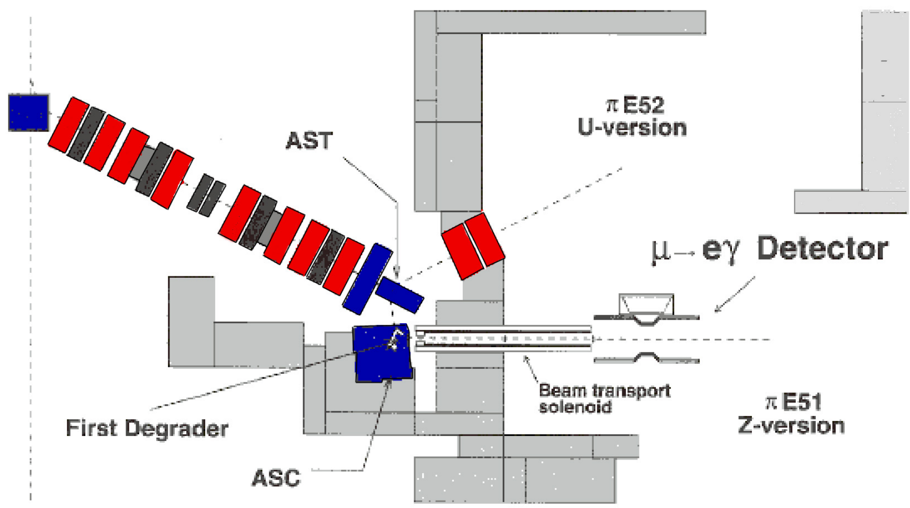

Figure 1: πE5 Beam line and experimental area showing the two branches, "U" leading to the πE52-zone and "Z" leading to the πE51-zone. The layout shown is as in the proposal. The blue elements depict bending magnets, while the red ones show quadrupole element. The grey elements depict beam safety elements as well as sextupole magnets.

Previous measurements on the "Z"-branch [4], showed that a suitable number of muons could be transported to a final focus with the help of a large aperture, 8.5 m long solenoidal magnet (PMC-magnet), after having passed a degrader to separate the muons from the contaminant beam positrons.

A comparative study on the "U"-branch was started with a beam test, during the months of September and October 2001, which however, was prematurely ended by a technical problem in the primary beam-blocker system of the πE5 beam line. This study of the "U"-branch will be continued in a July 2002 with a further beam test as outlined below.

4.1 Measurement Principle

The measurement principle for the beam phase space and rate measurements is shown schematically in Figure 2, for the case of the last measurement in the "U"-branch. The principle is applicable for all setups.

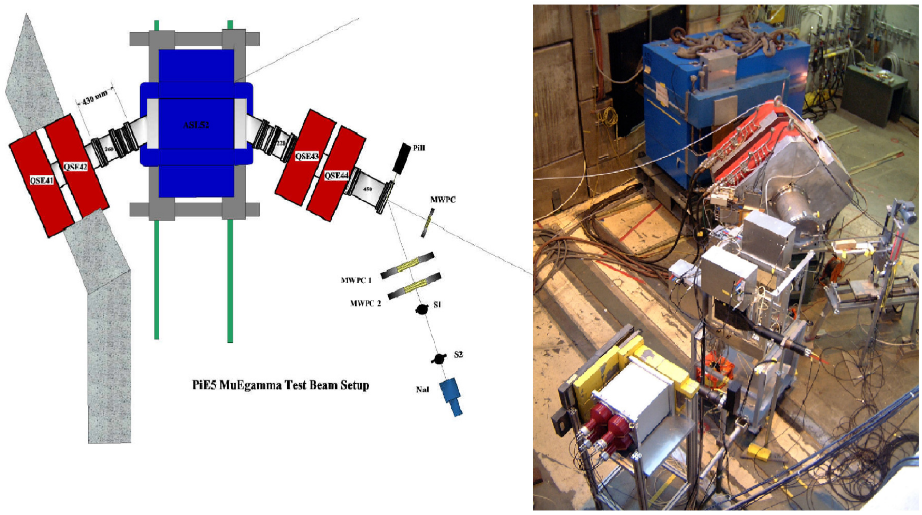

Figure 2: "U"-branch area layout, schematic and photograph, showing the spectrometer, consisting of the quadrupole doublets QSE41/42 and QSE43/44 as well as the dipole magnet ASL52, which was mounted on a moveable assembly, running on rails, in order to gain access to the specially designed degrader system. The degrader was located upstream of QSE41 and is not shown in the figure. A 4-micron thick differential pressure window, made of Mylar was placed just after QSE42 in order to suppress rest-gas activation in the spectrometer. Also shown are the detector systems used, a small "pill" scintillation counter, mounted on an X-Y scanner. A scintillation counter telescope S1,S2, together with a large NaI(Tl)-counter. A set of fast multi-wire proportional chambers (MWPC1/2), used for tracking, and a profile MWPC.

Measurements were taken at two locations in the area, namely, at the entrance, immediately downstream of the QSE42 quadrupole magnet and at the exit window of the spectrometer, some 50 cm after QSE44. In total, thirty-one measurements were taken under different conditions (counter type, beamline tune, momentum byte, collimator size and degrader in/out). For the degrader measurements, a foil of 450 microns of Mylar was used to separate the initial 28 MeV/c surface muons from beam positrons of the same momentum. While the positrons were virtually unaffected by the degrader, the muons reached a central momentum of close to 23 MeV/c, with still sufficient residual range to exit the final vacuum window without stopping, see Figure 3. For all measurements a 2 mm thick, CH_2-collimator with either a 50 mm or 80 mm diameter hole was located at the same point as the degrader foil. This was used to force a higher vertical divergence of the muons at the degrader during beam tuning. Unfortunately, planned measurements without this collimator could not be carried out in the end due to the technical problems with the beam line. For more details concerning the measurements see [5].

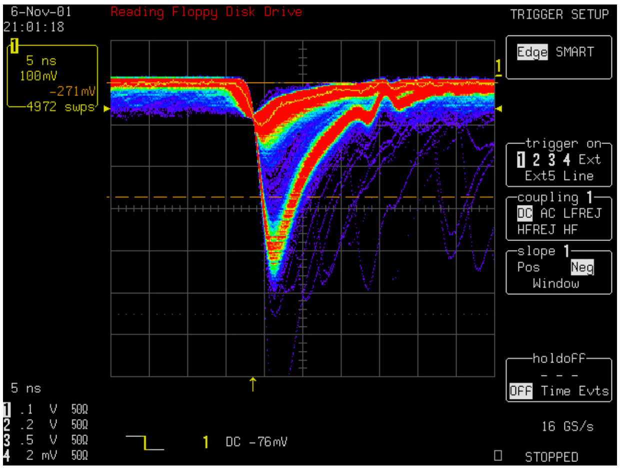

Figure 3: Digital oscilloscope output from a 1mm diameter "pill" scintillator, wrapped with only 25 microns of Aluminium and positioned after the spectrometer, showing a positron line (lower red distribution) and a muon line (upper red distribution). The intensity is proportional to the colour, red being the highest intensity.

4.2 Comparative Results

Table 2 below gives an overview of the comparative rate quantities obtained from the last "U"-branch and previous "Z"-branch measurements, using a degrader in both cases for separation and moderation. All quoted results, unless otherwise stated, are normalized to 1800μA of beam current on a 6cm long Target E and a momentum byte of 6.4% FWHM.

Table 2: Table 1.5 Comparison of "U"- and "Z"-branches for various conditions

Condition	"Z"-branch	"U"-branch
No Degrader, Transmitted to Zone	$3.6{\cdot}10^8 \mu^+ s^{-1}$	$3.5{\cdot}10^8 \mu^+ s^{-1}$
	$6.0{\cdot}10^8 \mu^+ s^{-1}$	$1.6{\cdot}10^9 \mu^+ s^{-1}$
Degrader, at Final Focus	$2.0{\cdot}10^8 \mu^+ s^{-1}$	$3.2{\cdot}10^7 \mu^+ s^{-1}$
μ/e ratio at Muon Peak	9	16.5

The main points are listed below, for a more detailed evaluation see [5]. The transmitted surface muon intensities in both of the πE5 branches are equivalent without a degrader, however, the beam positron contamination seems to be a factor of 2.7 times higher in the "U"-branch. The use of a spectrometer in this branch causes a loss of about a factor 2.1 in muon intensity, irrespective of condition.

The situation with the 450 micron Mylar degrader showed a dramatic loss in muon intensity of a factor 5.5, already in front of the spectrometer. This loss, although not expected, was attributed to the increased vertical divergence introduced by the multiple scattering of the degrader foil together with the smaller aperture (r$\sim$12.5 cm) of the QSE41/42 quadrupole doublet, compared to that of the rest of the beam line, i.e. QSFs (r$\sim$20 cm). The absolute rate at the final focus compared with the "Z"-branch was more than a factor of 6 lower.

Analysis of data taken by scanning the muon beam spot, after the spectrometer, using a small pill-counter mounted on a remotely controlled X-Y table, shows that the separation quality, in the case of using the spectrometer in the "U"-branch, is very good. The results are shown in Figure 4, a total suppression factor of 90 was obtained, though with suitable collimation more than a factor of 300 could be envisaged without significant loss of muons.

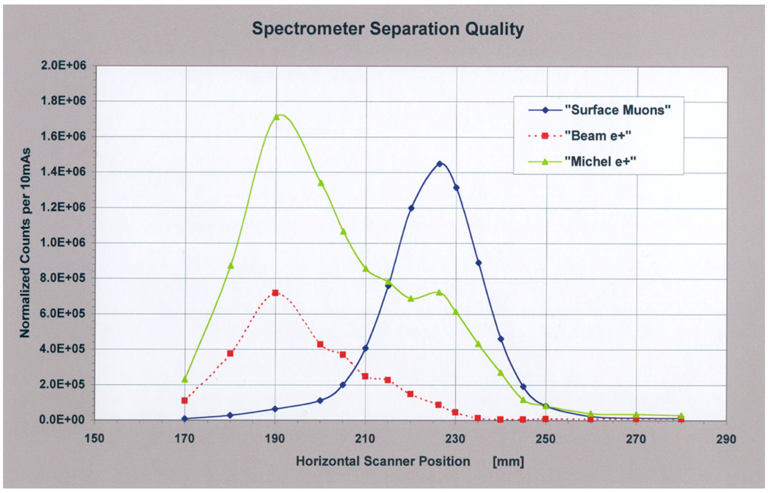

Figure 4: Offline results from a scan of the muon beam profile, post spectrometer, using a pill-counter. Shown horizontally is the scanner position in millimetres. Vertically the normalized counts are shown. The muon beam profile is shown relative to the contaminant positron distributions from beam positrons (red) and decay positrons i.e. Michel positrons (green). The positron distributions below x = 190 mm are cut-off due to the spectrometer acceptance. High beam momenta correspond to low x-value.

Owing to the large loss of muons with the degrader in place, an extra background of decay positrons was present and significant. Measurements suggest that a substantial part of these Michel positrons have their origin upstream of the spectrometer.

A muon momentum scan of the kinematic edge of pion decay (29.79 MeV/c), a check of the momentum calibration of the beam, was also undertaken, without a degrader. The results gave the central beam momentum as ~1.4% higher than the assumed value, with the resolution of the edge $\Delta P/P$, equal to 3.4% FWHM, equivalent to the selected momentum byte of the beam. A plot of the data, for the uncorrected momenta, is shown in Figure 5. The only feature of these data that do not match expectation is the momentum behaviour below the edge. This can clearly be seen in the figure, as the difference between the two curves, where the expected $P^{3.5}$ behaviour (red curve) is not follwed by the data points. A GEANT[6] simulation using the residual material in the beam line showed that the $P^{3.5}$ behaviour should be valid down to ~23 MeV/c. This effect will need to be checked in the next beam time. Following this, a linearity and offset check of all magnet power supplies was made, showing a good linearity for all devices with any offset in the few per mille range, and thus negligable.

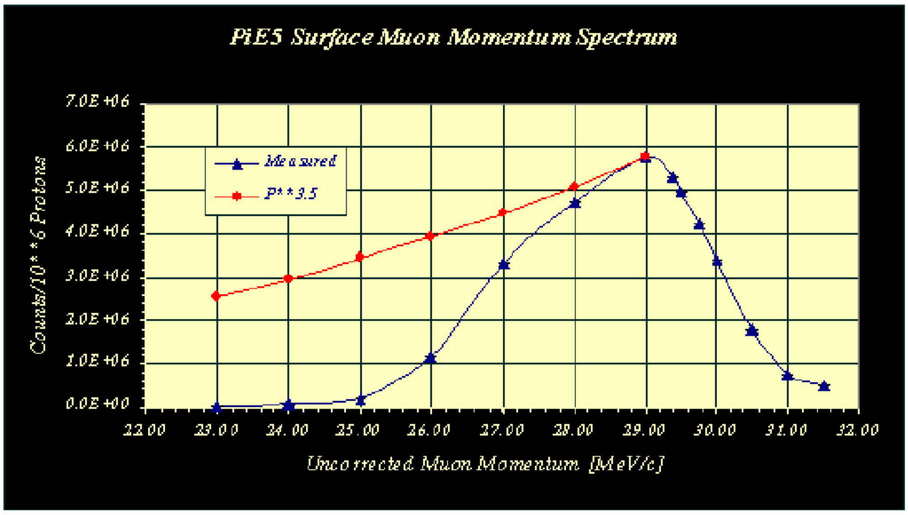

Figure 5: Beam momentum calibration, showing data from a scan of the kinematic edge in pion decay at rest, i.e. the momentum spectrum of the transmitted surface muons. From a fit to the edge a $\Delta P/P$ of 3.4% FWHM was obtained, verifying the set momentum byte of the beam. The central beam momentum was found to be 1.4% higher than expected. The measured data points are shown in blue, whereas the expected fall-off behaviour with momentum, i.e. $P^{3.5}$ is shown by the red curve.

4.3 Implications

The present results from the "U"-branch measurements, clearly show that the use of this beam line with a degrader placed at the focus of the AST sector magnet and followed by standard QSE quadrupole magnets in the shielded part of the beam line, gives both an unacceptable rate loss and a Michel positron background which is transmitted downstream. The solution to this problem will be tackled in the next beam time, July 2002, when measurements using a Wien-filter and a solenoid to simulate the final set-up are to be used, cf. below for further details.

Finally, concerning the "Z"-branch, it was shown in previous measurements that a suitable number of surface muons as well as a reasonable beam positron separation could be achieved with the large aperture, 8.5 m long PMC solenoid. However, since phase space measurements were not made in this branch but rather imposed through collimation, these measurements are outstanding if an optimal, short beam transport solenoid is to be designed for the experiment. It is planned to undertake these measurements in November 2002, such that all measurements, necessary for a decision as to which branch will eventually be used, can be made by the end of 2002. This should allow a final beam line design to be put forward in spring 2003, followed by a six-month construction and delivery period for the beam transport solenoid.

4.4 July 2002 Beam Test

As previously mentioned, the "U"-branch test will continue in July 2002, using a Wien-filter as a mass separator for the beam positrons and surface muons. The separation will be made vertically, thus optimally matching the small vertical source size at the production target.

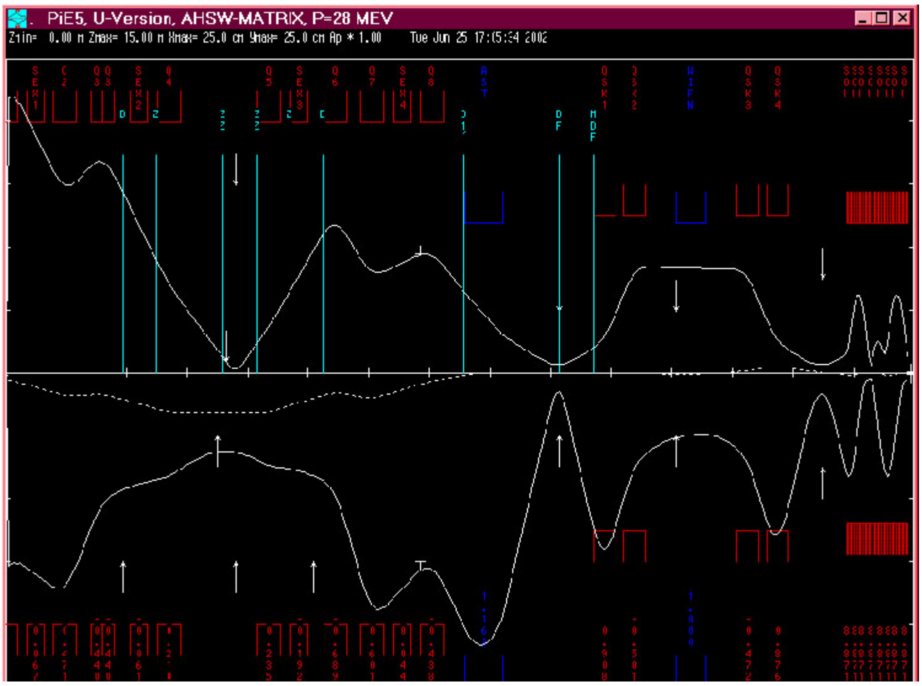

Figure 6: πE5 TRANSPORT beam envelopes (solid white lines) for the proposed Wien-filter set-up in the "U"-branch. The vertical envelopes are shown in the upper-half of the figure and the horizontal in the lower-half. The dashed line shows the momentum disperion trajectory for a 1 % higher momentum. The beam elements and their apertures are show in red and blue. The horizontal axis is in 1 m intervals along the central trajectory of the beam line, whereas the vertical scale is shown in 5 cm divisions.

A 1 m long solenoid will also be used in order to simulate the final experimental set-up. A simulation of the beam optics, as given by TRANSPORT[7] is shown in Figure 6. An image of the production target is made at the centre of the momentum defining slits, between Q4 and Q5, where the momentum dispersion is ~3.1cm/%. This point is again imaged to the fixed horizontal focus of the AST sector magnet, at the location DF, where the previous degrader foil was located. A point-to-parallel transformation is then made to the separator (WIEN), where the beam positrons will be deflected vertically. Then with a parallel-to-point transformation leading to a focus in front of the solenoid, where a collimator will be placed to ensure only the surface muons are transmitted. In the solenoid there is one intermediate focus for a degrader, followed by the final focus where the stop target will be placed.

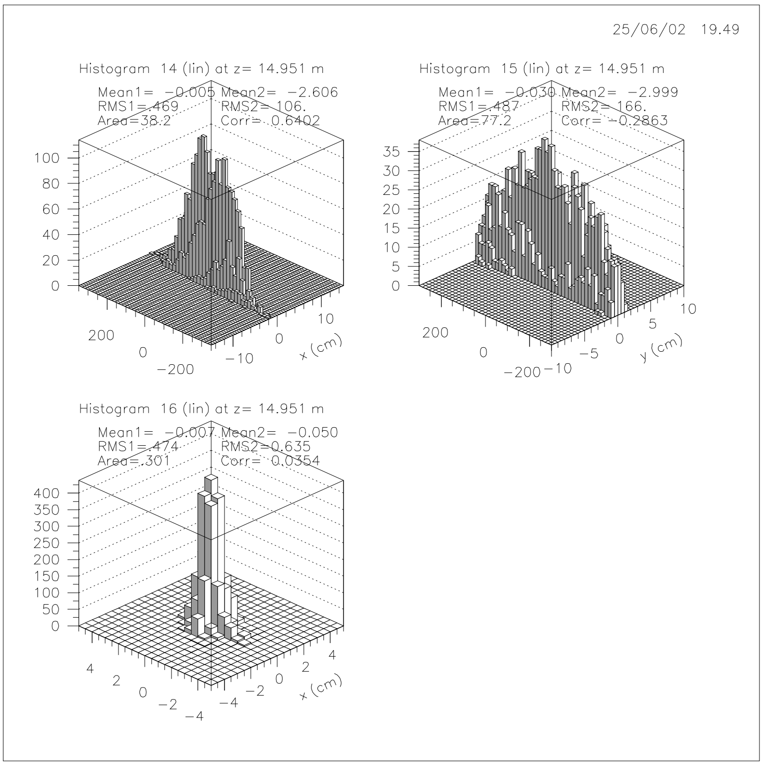

Figure 7: πE5 TURTLE 2^{nd}-order calculation output for the proposed Wien-filter set-up in the "U"-branch. The three histograms show the beam phase space 5 cm after the exit of the solenoid. The top-left shows the (x-x') phase space in cm·mrad, followed consecutively by the (y-y') and finally the beam spot size (x-y) in cms. The simulation is for a total of 20000 particles tracked through set-up, approximately 17% of the muons make it to the final focus, with more than 70% being lost up to and including the momentum slits.

A simulation of the set-up using the 2^{nd}-order ray tracing programme TURTLE[7] showed, cf. Figure 7, that for a total of $2{\cdot}10^4$ surface muons started, approximately 17% survive up to the final focus, and that the predominant loss of more than 70% occurs up to and including the momentum slits FS42. A separate simulation excluding the separator and solenoid and focussing just behind QSE42, at the entrance to the zone, gave a transmission of 21.5%. This value should be equivalent to the rate measured, without a degrader, at the same location in the October 2001 run cf. Table 2, i.e. equivalent to $3.6{\cdot}10^{8}\mu^{+}s^{-1}$. Using this value and scaling the above mentioned transmission of 17%, would correspond to a value of $2.7{\cdot}10^{8}\mu^{+}s^{-1}$ at the final focus, without any degrader in the solenoid.

The estimated phase space of the beam at this point, taken from TURTLE, gives an rms half-width of the horizontal and vertical profiles of σ_x = 5mm, σ_y = 6mm, with divergences in the horizontal and vertical planes of x' = 106 mrad and y' = 166 mrad, respectively .

Further calculations in progress or planned, include: the background effect of a degrader placed at the focus, in the centre of the solenoid; the effect of using minimal degrading combined with a lower central momentum; the effect on the beam optics of coupling the gradient field of the COBRA spectrometer to the transport solenoid; suitable collimation and shielding locations for optimal background suppression, as well as simulating the fate of non-stopped beam particles.

4.5 Target

So far, the main effort has concentrated on the beam optics side, with the basic concept of the target outlined in the proposal [1] as the basis for the stopping of the muons. The materials used in the beam tests so far have been Mylar for the degrader and Polyethylene (CH_2) for the stopping material. The main reason Mylar was used was that it was already implemented for the beam windows and convenient thicknesses were readily available, while for the initial tests the somewhat worse properties were not seen as prohibitive. However, for a realistic measurement, the best possible material should be chosen.

Assuming a central beam momentum of 28 MeV/c, with a momentum byte of 6.4% FWHM, a materials simulation was done using the GEANT[6] code. Three suitable target/degrader materials were looked at: Polyethylene $CH_2 = CH_2$, Mylar $C_5H_4O_2$ and Kapton $(C_{22}H_{10}N_2O_5)_n$. The mean range was found to be 1113 microns in the case of CH_2 and ~870 microns for both the other materials, with the range straggling varying between 7.8% and 8.2% respectively. Assuming the same equivalent thickness of the target, as seen by the beam, and as in the proposal, a CH_2 target with a density of 0.95 g/cm^3, would have to be 150 microns thick, if placed at the same slant angle. This would imply a residual material thickness of 700 microns of Polyethylene as a degrader. In the case of Mylar the the respective thicknesses are 100 microns for the target and 600 microns for the degrader. This implies about 16% less multiple scattering for both muons and higher energy positrons in the degrader for the case of Polyethylene as well as 20% less equivalent material for the degrader. The radiation length X_0 in the case of Polyethylene is also about 12% longer than that of Mylar, giving a total of 30% less X_0s in the case of a CH_2 degrader.

Overall, it seems as though Polyethylene is the better material from both a background suppression and a beam quality point of view, however, presently questions such as the depolarization characteristics of these materials is being checked as well as starting a serious look into the mechanical suitability for constructing a zero-materials, infinite precision target suspension system. The experience and knowledge obtained by the previous experiments e.g. MEGA and the Crystal Box Collaborations, concerning the target questions and the use of special calibration targets has been duely noted and will also be taken into account at the appropriate time.

In conclusion, there are still many open questions concerning the beam line and target for the experiment. However, the strategy for answering the questions is clear. At this point in time, although the optics and the target design questions will be looked at in parallel, the emphasis is needed on the beam optics side, as these results direct influence the target design.

5 COBRA magnet

In this section the status of preparation for the COBRA magnet is reported. The design of the magnet including the mechanical design was finalized and construction of the magnet has been started. The details of the design are described in the separate report[8] which will be attached to this report.

5.1 Mechanical design of the COBRA magnet

Fig. 8 shows the coils, support shell of the coils, and cryostat. This design was optimized by the detailed mechanical calculations and related experimental tests which will be summarized here. The details can be seen in the technical note[8].

The stress in the coil due to the electromagnetic force is maximized around both edges of the support shell of the central coil. In order to reduce the stress around that region, a thin support cylinder bypassing over the central coil (bypassing support) is adopted as shown in Fig. 8. The shape and thickness of the support shell and bypassing support were optimized to make the mechanical stress acceptable for the materials used in the magnet. Fig.9 shows the calculated stress distribution around the central coil and bypassing support. The result indicates the maximum stress is 74 MPa at the edge of the support shell for the central coil which is well below the maximum allowed stress, 100 MPa at 4K for the aluminum (A5083P) to be used in the support shell.

Various mechanical tests for some essential parts in the magnet are being performed to verify the validity of the current design of the magnet.

The mechanical strength of the bypassing support which will carry the greater part of the axial force acting on the end coil and gradient coil was measured. A test cylinder with the same geometry as the bypassing support was used in this test. The measured buckling stress was 68 MPa. We can conclude that the supporting scheme using the bypassing support will work because the stress calculations predict the axial force acting on the bypassing support less than 44 MPa.

In order to test the strength of the glueing between the coil and aluminum support shell for the axial component of the electromagnetic force, a shearing tests using a small model coil(50 mmϕ and 42 mm length) glued to the aluminum support shell with an epoxy resin were also performed. Six samples with different thickness of the epoxy resin between the coil and support cylinder were tested at liquid nitrogen temperature. The average of the breaking stress is 7.8 MPa. The level of the breaking stress is almost acceptable and could be improved by using another type of insulating tape.

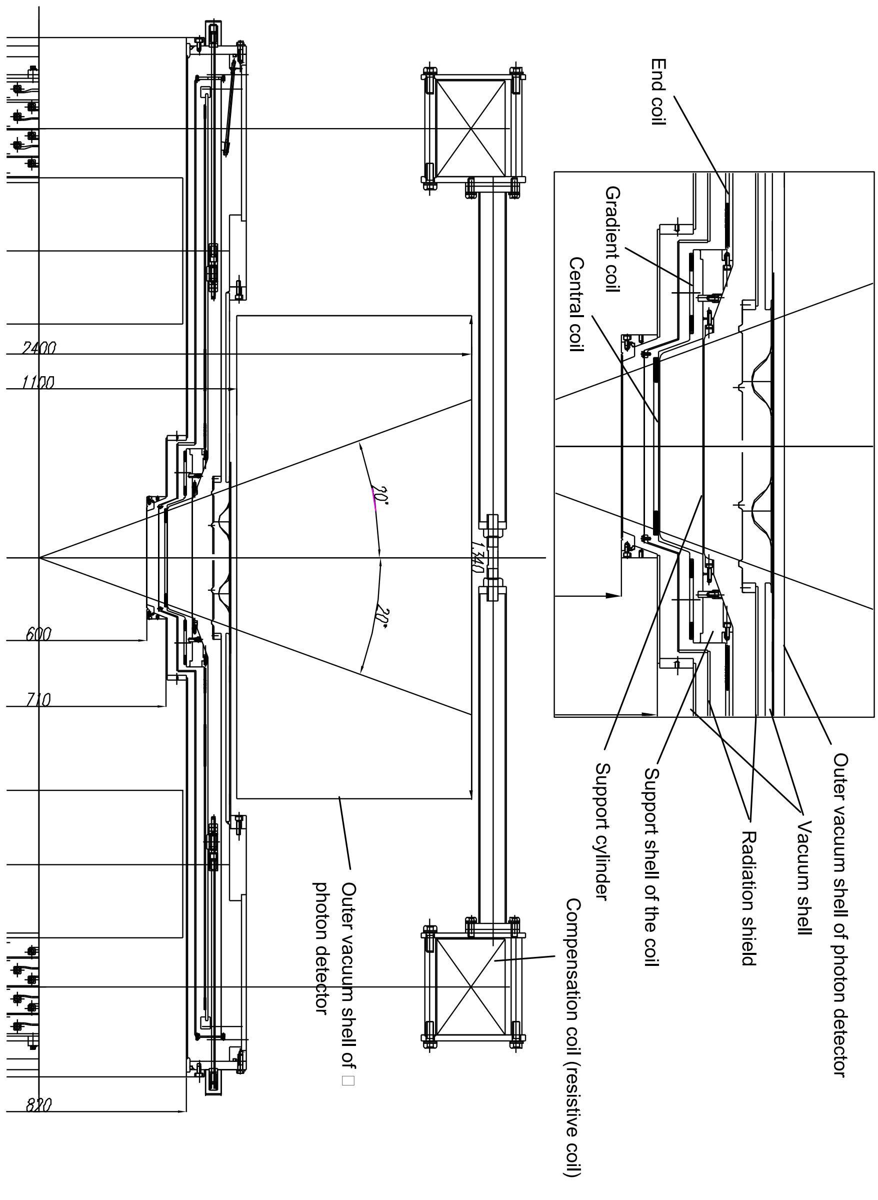

Figure 8: Design of the coils, support shell of the coils, and cryostat.

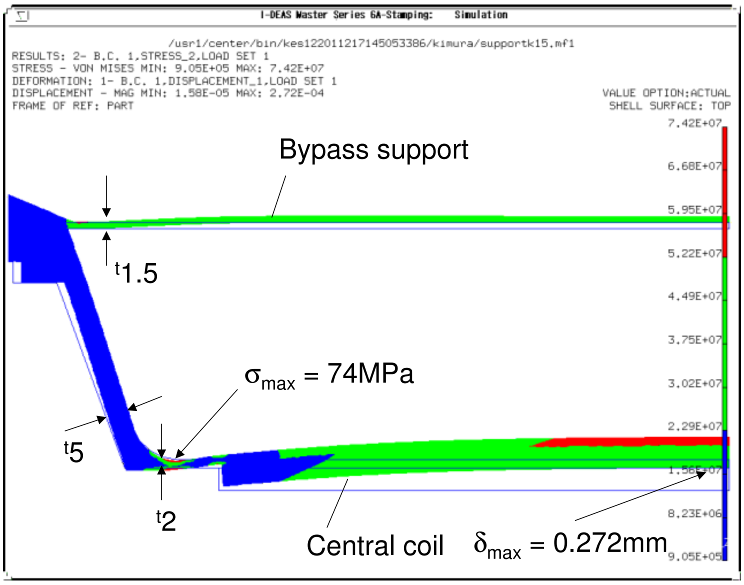

Figure 9: Stress distribution around the central coil of the magnet.

5.2 Changes of the magnet design since the proposal

The design of the COBRA magnet has been slightly changed compared to that described in the proposal. The major changes are as follows.

- A pair of the compensation coils is adopted to reduce the stray field in the vicinity of the photon detector.
- The step structure is adopted in the central region of the magnet instead of the sand-glass shape as described in the proposal.
- The coil radius is smaller by about 10 % to reduce the stray field.

The possible effects resulting from these changes have been investigated and briefly summarized here.

Since the coil radius is reduced by about 10 % compared to the design in the proposal, the strength of the central field has to be increased by about 10 % so that the tracking of the signal positron is properly performed. The performance of the positron spectrometer based on the current design of the magnet was studied and no problem was found as described in Ref. [8]. In order to minimize the increase of the operating current for increasing the central field strength, the superconducting cable was wound in the "edge-wise" way in the central coil instead of the usual "flat-wise" way. These two kinds of ways to wind the cable are illustrated in Fig.10. We can obtain the stronger central field by the edge-wise winding with the same operating current. However, if this winding way is adopted, we have to accept the increase of the material thickness of the central coil by $2.6 \times 10^{-2} X_0$. The details of the overall transparency of the coil are described in Ref. [8] and the effects on the efficiency of the photon detector are discussed in Sec.8.6.1.

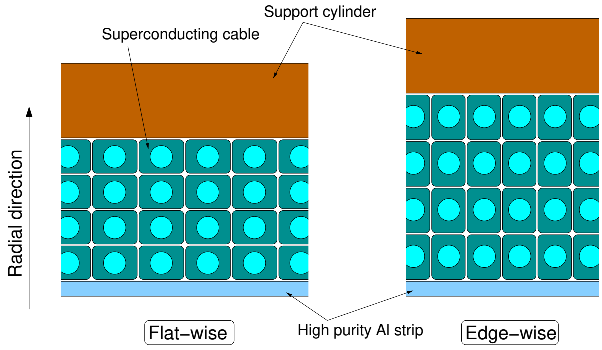

Figure 10: Flat-wise and edge-wise winding.

Since the magnetic field produced by the compensation coil is not so strong, the electromagnetic interactions of the compensation coils with the main superconducting magnet and beam transport magnet will be easily managed by the usual supporting structure as illustrated in Fig. 13.

In spite of the changes in the design of the magnet as listed at the beginning of this section, there is no significant change in the shape of the magnetic field distribution around the main magnet and beam transport magnet. Any strange behaviour of the muon beam and additional background source could not be found in the Monte Calro simulation. The same study should, however, be performed for a final design of the beam line.

In addition, we have stared the calculations of the magnetic field distribution under the more realistic conditions of the experimental area. Initially, the iron structure beneath the experimental floor were taken into account in the calculation. Such calculation requires a non axi-symmetric 3-dimensional modeling. The preliminary results indicate that the change in the residual field in the photon detector region is less than about 10 % and the changes in the muon beam parameters and performance of the spectrometer are negligible.

5.3 Status and prospects of the construction of the COBRA magnet

The design work including the mechanical design as described in Sec. 5.1 was finished and the construction has been started. The winding of the superconducting cables for the main magnet is in progress and some of the coils are already completed(Fig. 11). After the central coil and two gradient coils are completed, they will be assembled together with an aluminum support shell. This part is quite essential in the magnet because the current density is the highest in the magnet. An excitation test of this part will be performed prior to the assembly of all the coils in order to measure the various properties of the COBRA magnet such as the superconducting and mechanical characteristics. This test must be the next big milestone on the construction of the COBRA magnet. In the test the coils will be cooled down to around 4 K in a vacuum using a cold finger from a liquid helium tank. The property of the coils can be studied under the similar thermal condition to that of the real COBRA magnet where the coils will be cooled in the vacuum cryostat by using mechanical refrigerators. The excitation with an operating current 10 % larger than designed will be tried in the test. The test will be performed in this summer. Concerning the compensation coil, the winding of the hollow conductor made of copper was completed (Fig. 12). An excitation test of the compensation coils will be performed in this summer. The construction of the cryostat is also starting in parallel. All the components of the magnet will be assembled by the end of this year. The engineering studies on the scheme of the assembly and alignment of the magnet are starting. Fig. 13 illustrates the current design of the magnet assembly. After the assembly of the components, overall tests of the magnet will follow. After that the COBRA magnet will be shipped to the PSI around February or March in 2003. Magnetic field mapping will be performed after the installation at the PSI. The precise field map is indispensable to the reliable positron tracking. The field map will be made by means of a combination of the field measurements and the accurate calculations of the magnetic field.

Figure 11: Central coil of the COBRA magnet.

Figure 12: Winding of the compensation coils is completed.

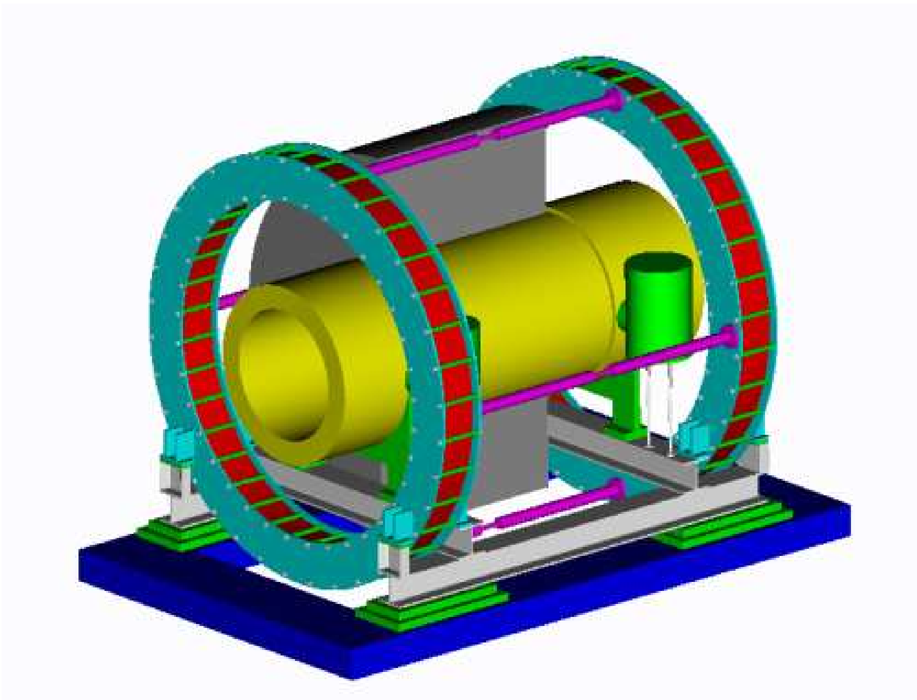

Figure 13: Current design of the magnet assembly.

6 Drift Chambers (DC)

To obtain information about the performance of the proposed chambers, two test chambers were built. The first in Tokyo [9], a classical square-framed construction, which demonstrated that the required precision stated in the proposal was, in principle, achieved using β-particles from a Sr^{90} source, cf. Table 3:

Table 3: Comparison of the obtained precision of the various resolutions and the proposal values, for the measurement conditions see [9]

Resolution given in σ from:	Tokyo	Proposal [1]
drift time measurement	100-150 μm	200 μm
vernier cathode measurement	425 μm	300 μm
charge division measurement	2 cm	1 cm
drift velocity and drift time	4-12 ns	5 ns

The measurements also proved that the necessary gas gain could be obtained for a variety of candidate gas mixtures. The mini-prototype built at PSI[10] (8 cm in length for the longer z-side, instead of 100 cm) has tested the mechanical solution of an open-framed chamber (without a frame on the target side) and confirmed the Sr^{90} results of the Tokyo measurements. The positional resolution obtained over a complete drift-cell is shown in Figure 14, resulting in 120 μm at

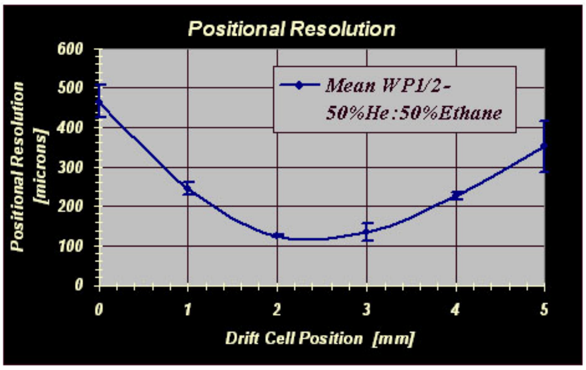

Figure 14: Positional resolution in microns, in the direction of the wire plane, measured across a drift-cell of the PSI mini-prototype chamber, using a Sr^{90} source and a scintillator telescope, as well as a double collimator sytem. A 50 vol. % Helium : 50 vol. % Ethane gas mixture, at a high voltage of 1900 V, was used.

the centre, for a high voltage of 1900 V and 50 % Helium : 50 % Ethane, by volume, gas mixture. The corresponding time resolution was found to vary between 5-12 ns over the drift-cell.

A bad matching of the wire, print and preamplifier impedances did not allow information on the precision of the charge division method to be obtained. However, the mini-prototype chamber was successfully operated in a 1 Tesla magnetic field using beam particles (e, π and μ) in a test in the πM1 area at PSI.

The following sections describe how the parameters of the final chamber will be optimised using two types of test chamber currently under construction. The first, the so-called 'Double cathode' test chamber and the second, the 'Charge division' test chamber, which will be used to optimize the positional resolution along the wire. Also described is how a 1:1 version of the cathode structure to optimise the vernier geometry will be built and so train the construction of the most critical part of the drift chamber. Finally, a detailed schedule of the tests and work to be done up to the end of 2003 are given.

6.1 Preamplifiers and Prints

In order to study the parameters of the drift chamber under ideal conditions and with maximum flexibility, a small board containing 3 channels of a new preamplifier has been designed. It fits the geometrical requirements of a preamplifier mounted directly on the frame of the final detector and allows an optimal impedance matching, important for the charge division measurement, to be made. Two channels of the preamplifier are shown in Figure 15 . A second stage of amplification outside the detector will also utilize the same chip. The board can also be optimally mounted on the print commonly used for both test chambers mentioned above. Software to simulate the effect of pulse reflection on the sensitivity of the charge division method have also been prepared.

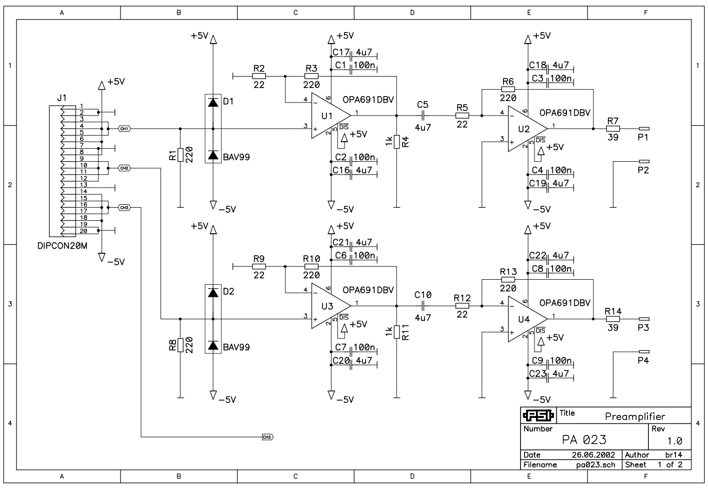

Figure 15: Layout showing two of the three channels of the new preamplifier board.

6.2 Double Cathode Test Chamber

The triple-strip vernier cathode as proposed[1] is not homogenous in position sensitivity. A Monte Carlo simulation, cf. Figure 16, has shown that a replacement of the middle, common cathode, by two separated double-strip cathodes for each chamber layer, only minimally affects the momentum resolution (0.9 % FWHM) and the efficiency (98 % →96.8 %). This replacement, will therefore allow, the use of the same double-strip vernier cathode (Figure 16) for each of the planes, though by shifting them by a quarter of the vernier period, relative to each other, the half-period ambiguity can be resolved and the homogeneity of the position sensitivity can be restored. A complete R&D programme will start in July with four small, square chambers (each of three cells, 6 cm long) equipped with cathodes, as described above, and read-out with the new prints and preamplifiers. This simple structure makes it easy to test different cathode structures (produced as prints on a 100 μm kapton foil). The size of these chambers is small enough to fit into a dipole magnet for measurement at 1 Tesla. The number of chambers allows the 'auto'-calibration of the positional resolution, using either cosmic muons without a magnetic field or with beam particles in a constant field. This set-up will enable the behaviour and gas properties in the magnetic field to be studied and the optimization of a number of chamber parameters such as: the distance between the two middle cathodes, the tails in the distributions for position and timing, as a function of efficiency and rate and the optimal period of the vernier structure.

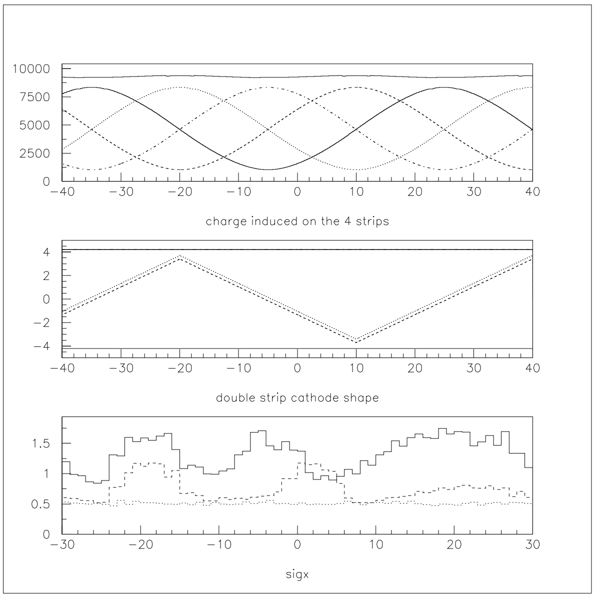

Figure 16: Results of a Monte Carlo simulation of the Vernier cathode pattern. With the shape of the double-strip cathode, as shown in the middle picture, the four induced charge dependences shown in the upper picture are obtained. The lower figure shows a comparison of the positional resolution for the two double-strip cathodes (dotted line) with that of two versions of the triple-strip cathode, the first, the proposed geomety (solid line) and the other, an optimized one (dashed line). The horizontal axis shows the distance along the wire, while the vertical axis shows the resolution in millimetres.

The required good gas tightness and the open-frame geometry complicates the construction using O-rings. Various materials and techniques to tighten the chambers externally with glue (e.g. THREE BONDS 1350) have been studied; such solutions, which would dramatically simplify the construction of the chambers and significantly reduce the costs, will be tested on the small chambers.

6.3 Charge Division Test Chamber

A 1 meter long, simply constructed chamber with three anode wires, equipped with the same prints and electronics as the 'Double cathode' test chamber is under final construction and will be used to optimize the anode read out. It will also allow the comparison of different wire materials (e.g. Steel wires 1200 Ω /m) with tungsten wires (330 Ω /m).

6.4 Cathode Hood

The shape of the cathode on the open-frame side has also to be studied. It was found that a lengthening of the chamber, towards the target, by adding a dummy cell, simplifies the construction and ensures a non-distorted electric field configuration in the active volume. As far as possible, the use of support structures, which would increase multiple scattering and create dead regions, will be avoided. To get the necessary strength, the $12\,\mu$m thick cathode foil will be pre-tensioned and inhomogenously deformed. This deformation must be measured and if necessary, create cathode structures which are not straight in their original free state but straight once mounted. For this reason, the highest priority will be placed on making a practical final design of the cathode mounting tools and of the cathode supporting frames (Hood), with the goal of ordering these parts before the remaining parts of the first 1:1 prototype.

6.5 Software Development

One important and time consuming task is the development of software for efficient pattern recognition in a high rate environment and for the trajectory-fit in the non-uniform magnetic field. Preliminary work only has be done for the Monte Carlo study. The detector group, which is responsible for the construction of other detectors (POLDI, μ H-capture TPC) has been weakened in terms of manpower, as a result of the long period of time needed to replace the second physicist position in the group. This situation explains why very little effort could be placed on software development up to the present time. The POLDI detector is now in use and the largest development effort (the TPC) was recently brought to a close with a successful test. The manpower situation has also been resolved, with the appointment of a second physicist to the group in October 2002.

Table 4: schedule

Apr-Sep.02	Design prototype 1:1
Jul.02 Small	cathode chamber with prints 1m charge division chamber with prints 60 preamps $\Longrightarrow$Gas tightness test with "Threebond 1530"
Jul-Aug.02	Design and order second stage amplifier
Jul-Sep.02	Cosmic and source test $\Longrightarrow$Optimisation of cathode shape $\Longrightarrow$Tails in position and time resolution without Field optimisation of prints and wires
Sep.02	Order of prints prototype 1:1
Jul.02	Order of 1 set cathode
Jul-Aug.02	frames Construction of cathode mounting tool
aug-Oct.02	Test of cathode mounting $\Longrightarrow$Design of corrected cathode shape $\Longrightarrow$Test of open frame design
Oct.02	Delivery second stage amplifier
Sep-Oct.02	Order of cathode foils Order of prototype 1:1 frames
Oct.02 -Aug.03	Software development for Pattern recognition algorithm $\Longrightarrow$Trajectory fit in non-uniform magnetic filed Effect of accidental hits on reconstruction efficiency $\Longrightarrow$Determination of exact geometrical acceptance
Oct.02 -Jan.03	Delivery prototype 1:1 frames Delivery cathode foils Construction prototype 1:1
Oct.02 -Mar.03	Test of small prototype in 1 Tesla and beam $\Longrightarrow$Gas optimisation
Dec.02 -Feb.03	Test prototype with preamp, amplifier and FADC prototypes $\Longrightarrow$Final design
Jan-Mar.03	Order of frames and prints, order of preamps and amplifiers
Feb-Apr.03	Delivery of frames and prints Delivery of preamps and amplifiers
Feb-Aug.03	Construction of chambers

7 Timing Counter

This detector is designed to measure the positron timing with a resolution of 0.1 ns FWHM and to be used in the trigger for selecting events containing a positron coincident in time and direction with a photon identified in the electromagnetic calorimeter.

It consists of two superimposed layers of scintillator bars (see fig.19) each one 5 cm wide and read at each side by one fast PMT. For one of the two layers (the outer one) the scintillator bars are parallel to the beam direction (Z-axis) in order to minimize the effect of the magnetic field on the PMTs. This layer will be used for the timing measurement.

In the other layer the scintillator bars are bent in a circular shape and oriented perpendicularly to the Z-axis. This scintillator layer will be mainly used in the trigger for reconstructing the initial direction of the positron by measuring the Z coordinate of the positron impact on the timing counter. It will also be used for tracking redundancy.

PMTs are protected from the helium contained in the Drift Chambers gas mixture by means of a plastic bag in which nitrogen gas is flown.

First beam tests of this detector prototypes were made at KEK in 1999 [11] and repeated at Pisa in 2001 [12] by means of cosmic ray muons.

Several timing counter prototypes were built and tested: made of 1 m long BC404 scintillator bars (cross section 5 cm $\times$ 1 cm), wrapped with 50 μm of aluminized Mylar and coupled to PMTs through light guides at the two opposite ends.

We used Philips XP2020 UR ($2''\phi$, 470 ps transit time spread) or Hamamatsu R5946 fine mesh ($1.5''\phi$, same t.t.s. as the Philips ones) PMTs and tested several shapes of light guides.

The timing properties of these detectors were studied at Pisa by means of cosmic ray muons. Since the rate of these muons is relatively low and it is necessary to correct for position dependent effects, we set–up a telescope made of eight Microstrip Gas Chambers[13] (the same devices tested at PSI for the CMS experiment), four of which with strips at a small angle (5.7°) with respect to the other four, for stereo reconstruction of the muon tracks (see Fig.17). The dimensions of each chamber are 10 cm $\times$ 10 cm. The impact point of one muon along the counter prototype was reconstructed with a resolution better than 1 mm.

The muon timing (relative to a reference counter) is independently measured by each of the two PMT's of the counter, after correcting for "time walk" effects. As shown in Fig.18, the weighted average of the two measurements turns out to be $\approx$ 60 ps, independently of the position along the counter. Measurements were also performed by tilting the counter to increase the muon path and energy deposit. We checked that the timing resolution improves with the square root of the total number of photo-electrons.

We used a Montecarlo simulation to take into account the positrons trajectories in the final experiment in order to select the relative position and the thickness of the two layers of scintillator of the timing counter.

We find that a 40 ps timing resolution ($\Delta t_{\mathrm{fwhm}} \sim 100$ ps) requires a minimum of 5 MeV energy deposit in the scintillator. A good detector configuration is obtained by using a 0.5 cm inner layer (for triggering purposes) and a 2 cm outer layer (the one for the timing measurement). We evaluate a $\sim$ 94% positron

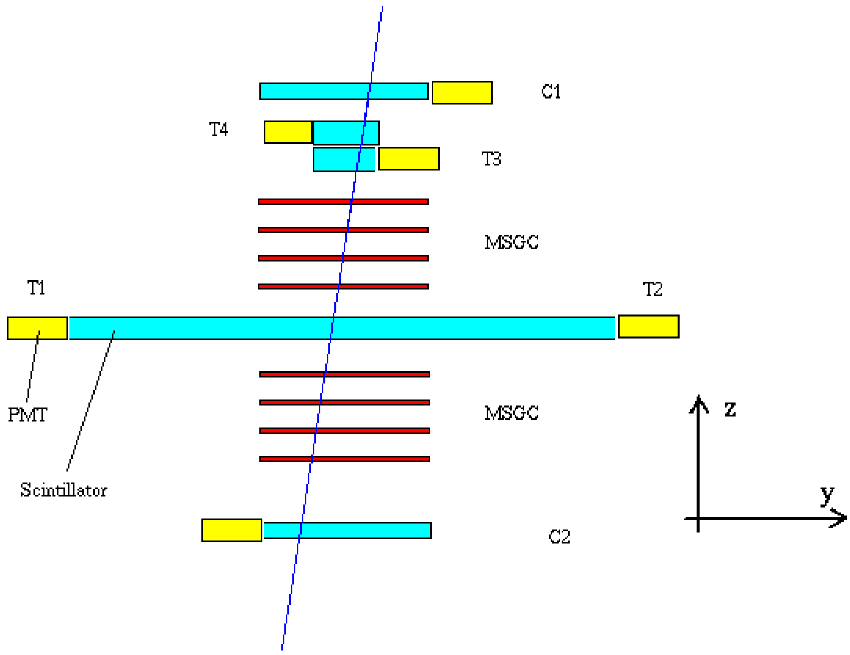

Figure 17: Layout of the MSGC tracking system for Timing Counter studies.

efficiency for such a detector configuration and a 5 MeV deposit in the layer used for the timing measurement.

The rate in the timing counter due to Michel positrons ill be about 2.5 MHz and should not constitute a problem for the operation of this device. We must obviously take care that other sources of background do not significantly increase the occupancy of this detector.

The engeneering study of the timing counter is in an advanced state. A 3D mechanical drawing of the detector is shown in fig.19. The axis of the outer layer PMT's can be kept below 10° relative to the direction of the magnetic field lines.

We plan to study the timing resolution of the R5946 PMTs in high magnetic field environments though similar studies for similar PMTs were already made by other collaborations[14] finding an insensitivity of the PMT timing response for magnetic fields along the PMT axis up to 1.6 T.

We estimate that the construction of this detector takes about one year. The final design of the timing counter could be ready for the beginning of 2003.

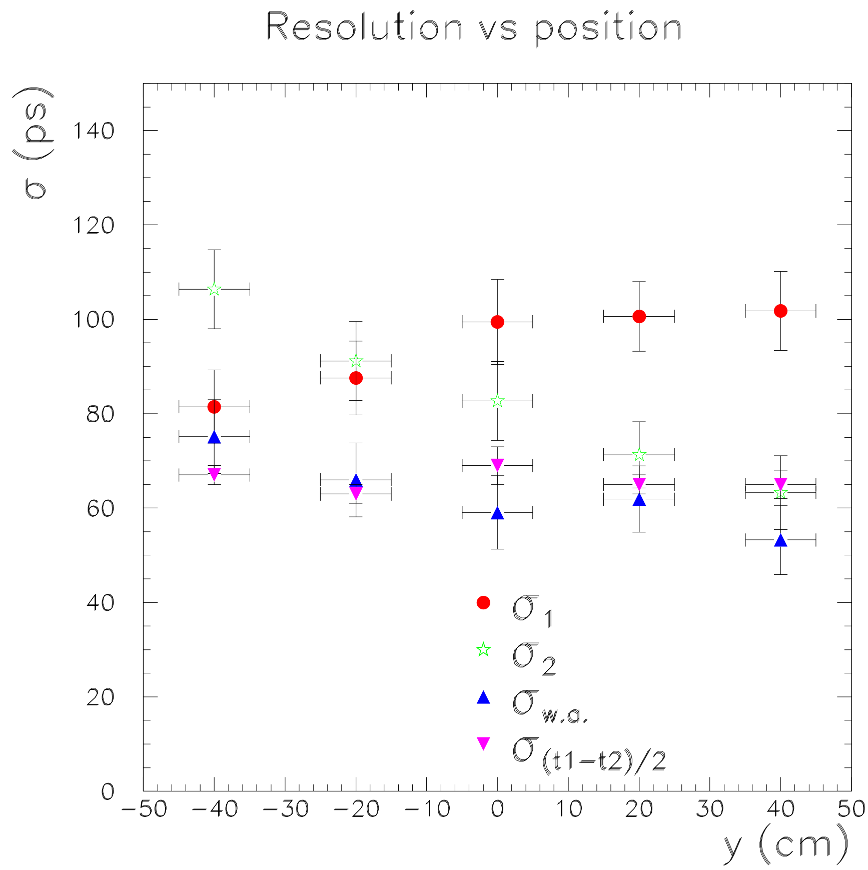

Figure 18: Timing resolution along the counter.

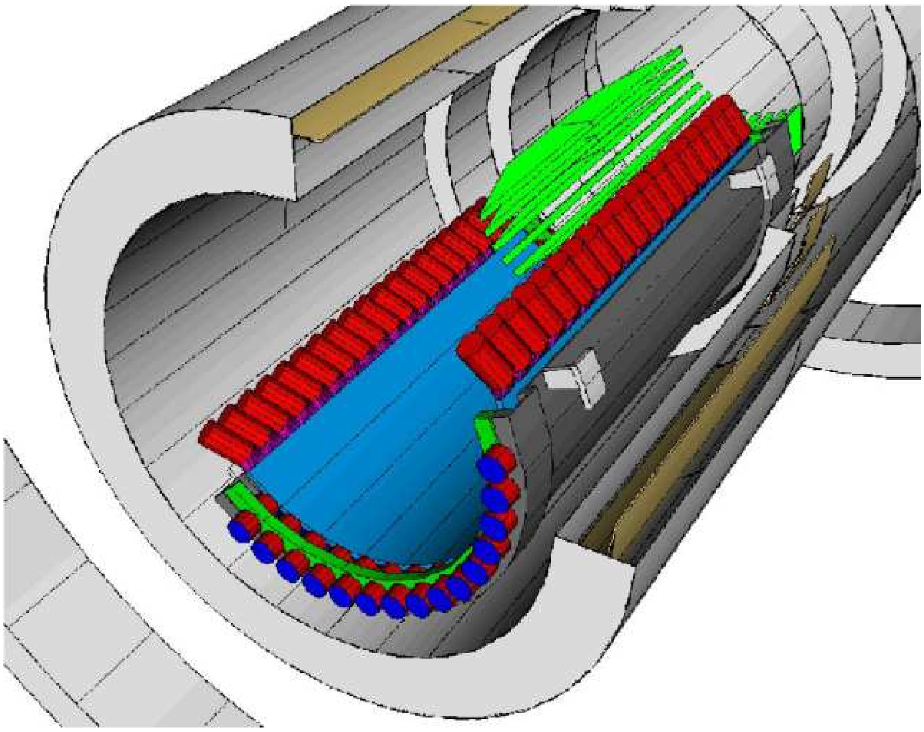

Figure 19: 3D mechanical drawing of the Timing Counter.

8 Photon detector

R&D works on the photon detector has been performed using the large prototype. The detector response has been investigated using 40MeV gamma beam, cosmic rays, and alpha sources. While performing these tests, it was found that absorption length (λ_{abs}) of scintillation light in liquid xenon in our detector was shorter than 10 cm due to remaining water of the order of ppm. Because of this contamination we had not been able to detect sufficient amount of scintillation light as we expected. For removing the contamination we introduced a purification scheme into the gas system and succeeded to achieve the λ_{abs} of $\sim$100 cm by circulating xenon through the purifier.

In this section, we report the results obtained in the last gamma beam test. The purification system newly equipped in the large prototype will be described. Then we report the newest results obtained using cosmic rays and alpha sources with purified xenon. Possible calibration methods of the PMT are mentioned. Status of other R&D works related to the photon detector will also be described.

8.1 The large prototype

Details of the large prototype are described in [5]. The schematic view of the detector is shown in Figure 20. A rectangular box onto which 228 PMTs are assembled is installed into a chamber with a thermal insulation vacuum layer. The active volume of the detector is 67 liters. A pulse-tube refrigerator is installed on the top of the chamber to recondensate xenon. A liquid nitrogen cooling pipe is equipped to help the refrigerator when more cooling power is required such in a case of liquefaction. Usually we use 120 liters of liquid xenon for detector operation. There are four ^{241}Am alpha sources and eight blue LEDs placed on the wall of the holder for PMT calibration. Detector operation has been tested for more than 100 days in total. Almost all components have been proved to work stably in liquid xenon environment except for a few ones such as PMT filler reported in the previous report.

8.1.1 Gamma beam test at TERAS

A gamma beam test was carried out in Feb. 2002. The electron storage ring (TERAS) in AIST, Tsukuba in Japan was operated at the maximum electron current of 200 mA around the nominal beam energy of 762MeV. Laser light of 266 nm was fed to the head-on collision point to induce inverse-compton scattering for providing gamma beam up to 40 MeV. There were two collimators between the collision point and xenon detector for defining the spot size on the detector face and removing low energy background. The schematic view of the gamma beam line is shown in Figure 21. The detector was moved with respect to the beam incident position for studying the position dependence of the detector performance. For triggering cosmic-ray events, 3 pairs of scintillation counters (TC1, TC2, and TC3) were placed as shown in Figure 22.

Figure 23 shows a calculated gamma-beam energy spectrum which includes all parameters of the laser system, electron storage ring, and geometry of collimators. The compton edge at 40 MeV is used for evaluating the energy resolution of the detector.

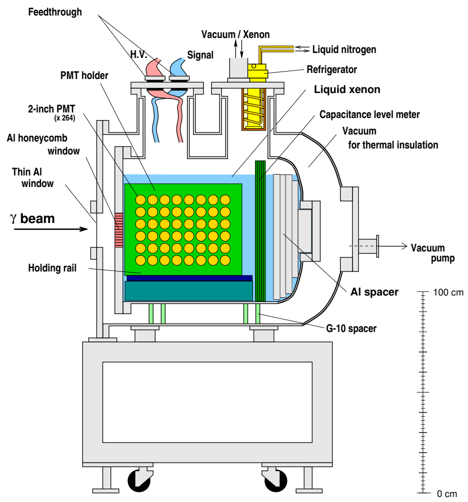

Figure 20: Schematic view of the large prototype.

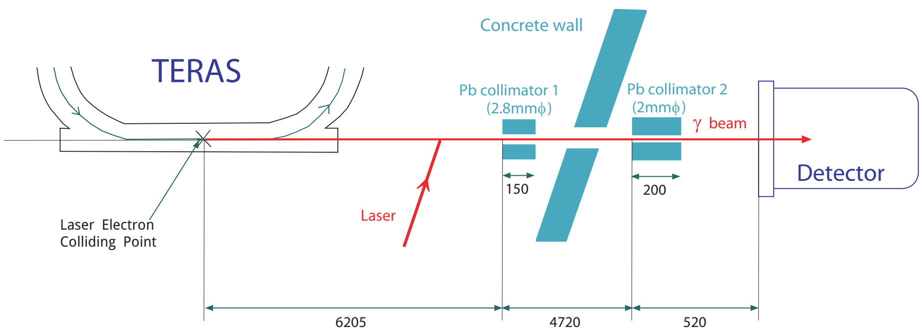

Figure 21: Layout of TERAS

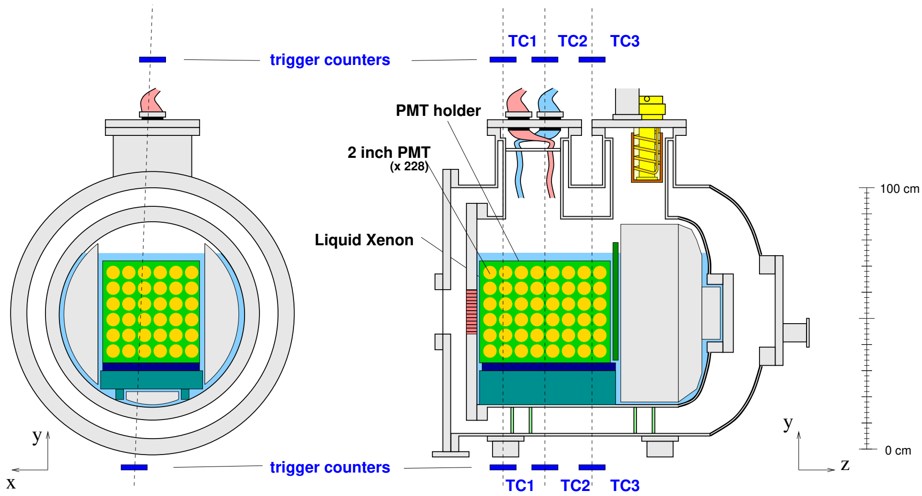

Figure 22: Trigger counters for cosmic-ray trigger.

Liquefaction of xenon was done prior to the beam time. The detector was evacuated to 2.0×10^{-2} Pa and then gas xenon was filled in the chamber up to 0.2 MPa. The chamber and the detector was pre-cooled with the refrigerator and liquid nitrogen cooling pipe down to around 165 K. After that liquid xenon is accumulated in the chamber by continuously supplying and liquefying xenon with the cooling system. After liquefaction, liquid xenon was kept at a stable temperature (163 K) and stable pressure (120 kPa) with the refrigerator. During the detector operation for 14 days, the temperature was stabilized in $\pm$ 0.1 K and the pressure drift was kept less than 1%.

8.1.2 Calibration of the PMTs

There are 8 blue LEDs equipped on the holder for PMT gain calibration. The LEDs were pulsed at 100 Hz by an LED driver with continuously adjustable driving voltage. Trigger signal was supplied from the same clock generator for the LED driver. 2 out of 8 LEDs were pulsed simultaneously for standard gain calibration and the other combinations were used for systematic error estimation of the calibration. 50k events with 5 different LED amplitudes were recorded in one calibration process. The standard deviation of ADC spectrum (σ_{ADC}) depends on the number of photoelectrons (N_{pe}) observed by the PMT:

$$\sigma^2_{ADC} = \sigma_0^2 + \frac{\overline{ADC}^2}{N_{pe}} \tag{1}$$

where $\overline{ADC}$ is the mean value of the ADC spectrum and σ_0 is a combined standard deviation of such as instability of LED voltage, temporal pedestal variation, etc. The variable N_{pe} is expressed in terms of gain of the PMT (G) as:

$$N_{pe} = \frac{\overline{ADC} \times C}{e \times G} \tag{2}$$

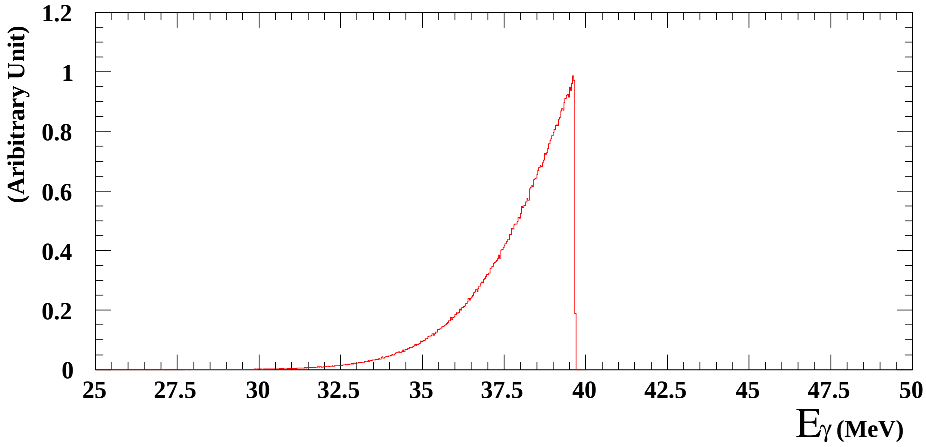

Figure 23: Calculated gamma-beam energy spectrum at TERAS.

where C is the least count of the ADC, 200 fC, and e is the electric charge of an electron. ¿From these two equations σ^2_{ADC} is written as:

$$\sigma^2_{ADC} = \sigma_0^2 + \frac{e \times G}{C} \times \overline{ADC} \tag{3}$$

The variance σ^2_{ADC} is proportional to $\overline{ADC}$ and the gain of the PMT can be evaluated from the slope parameter. Figure 24 shows an ADC spectrum for a typical PMT and in Figure 25 is shown an example of the relation between σ^2_{ADC} and $\overline{ADC}$. By fitting the relation with a linear function, gain of the PMTs was evaluated and adjusted to 10^6 at the start of detector operation. Calibration data were taken usually 3 times a day during detector operation.

The reproducibility of the calibration is estimated to be $\sim$1%. Systematic study using different combinations of LEDs shows that gain adjustment accuracy ranges 1% to 4% and 2% in average. Details of the gain calibration are summarized in a separate note [15].

For correcting the difference of effective quantum efficiencies of the PMTs, calibration data was taken for alpha events in low temperature gas xenon. Since the effects of absorption and scattering are expected to be negligibly small in gas xenon, light transmission can be easily simulated considering the geometrical configuration. PMT output spectra were fitted with a convolution of the Poisson function with a Gaussian and compared with MC prediction for evaluating the quantum efficiencies of the PMTs. Distribution of the obtained quantum efficiencies is show in Figure 26. Details of the analysis are described in a separate note [16].

8.1.3 Noise level measured at the large prototype

The noise level on all calorimeter channels becomes a critical factor if one has to sum several hundred channels to determine the shower energy in our unsegmented photon detector. To investigate the situation, several noise measurements were made. To separate the total noise (TN) into random noise (RN)

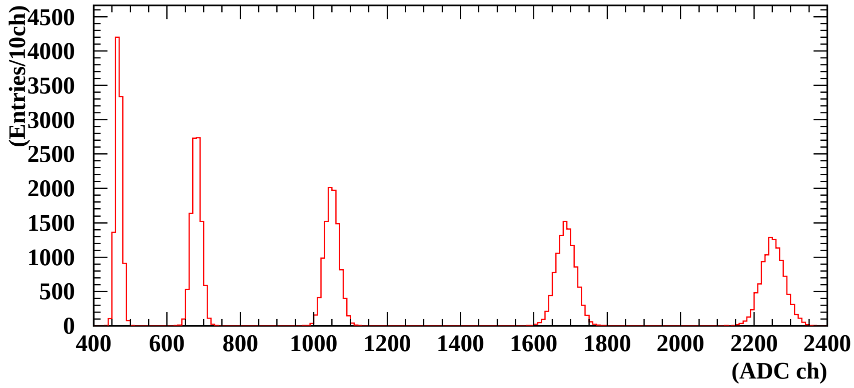

Figure 24: ADC spectrum of a typical PMT in LED calibration.

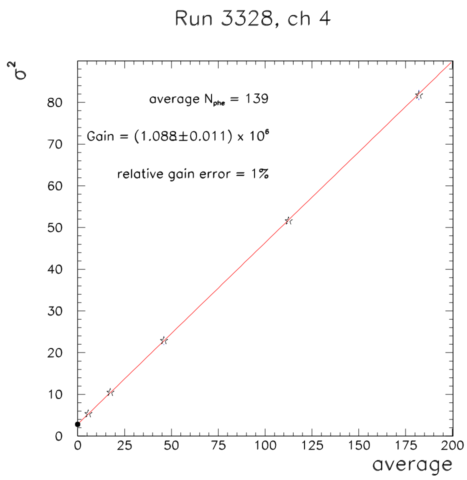

Figure 25: Example of the relation between σ^2_{ADC} and $\overline{ADC}$ in LED calibration.

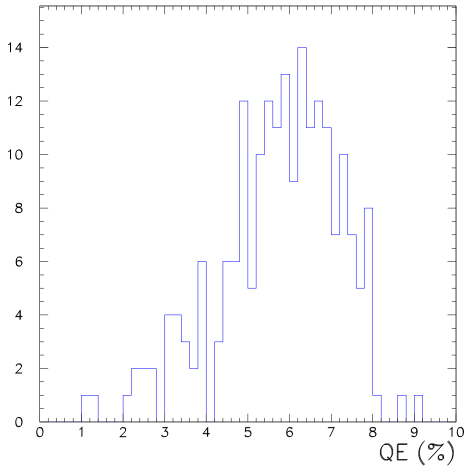

Figure 26: Distribution of quantum efficiencies evaluated using gas xenon data.

and common noise (CN), all even and odd channels were summed on an event-by-event basis.

$$S_{even} = \sum_{i=2,4,6,\ldots} ADC_i$$

$$S_{odd} = \sum_{i=1,3,5,\ldots} ADC_i$$

Then the difference and the sum of both values was calculated as

$$RN(k) = S_{even}(k) - S_{odd}(k)$$

$$TN(k) = S_{even}(k) + S_{odd}(k)$$

and histogrammed, where k is the event number. Any noise component which is common to all channels will cancel in the subtraction. Thus the RMS or σ of the distribution $RN(k)$ describes the random (incoherent) noise, while the RMS of $TN(k)$ contains the total noise. Since the squared sum of the random noise $\sigma(RN)$ and the common noise $\sigma(CN)$ equals the total noise $\sigma(TN)$, the common noise can be calculated as

$$\sigma(CN)^2 = \sigma(TN)^2 - \sigma(RN)^2$$

The result of such a measurement is shown in Fig. 27. The offset of $TN(k)$ comes from a imperfect pedestal calibration. Since the pedestal values for each ADC channel are currently only calculated with a precision of one bin, the sum of 224 channels shows a non-zero offset.

To convert ADC channels into energy E in MeV, following formula is used:

$$ADC[channel] = \frac{N_{pe}}{MeV} \cdot E[MeV] \cdot e \cdot g_{PMT} \cdot \frac{1}{Q/channel} \cdot A$$

where the number of photoelectrons per Mev N_{pe} is 875[2], e is the electron charge ($1.6^{-19}C$), the PMT gain g_{PMT} is 10^6 and the ADC sensitivity

[2]This number comes from the energy reqired to produce one photon in LXe (24eV), the photocathode quantum efficiency (6%) and the PMT coverage of the fiducial volume (35%)

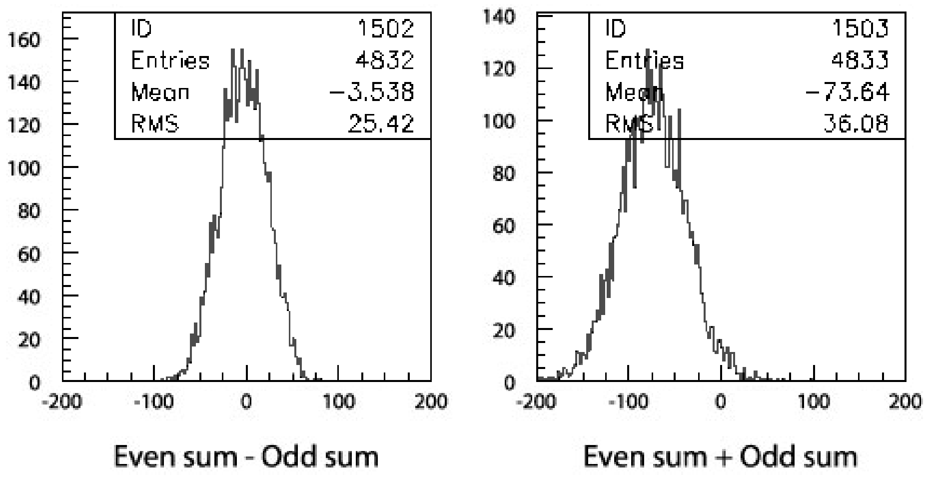

Figure 27: Distribution of $RN(k)$ (left) and $TN(k)$ (right) measured by adding all 228 channels of the large prototype. The x-axis is in ADC units.

$Q/channel$ is $200fC/channel$. The attenuation $A = 0.5$ comes from the passive splitter used. Reversing this formula gives

$$E[MeV] = 0.0025\frac{MeV}{channel} \cdot ADC[channel]$$

The noise becomes therefore $\sigma(TN) = 0.09MeV$, $\sigma(RN) = 0.06MeV$ and $\sigma(CN) = 0.06MeV$, which gives a negligible impact of 0.4% (FWHM) to our energy resolution at 52.8 MeV.

8.1.4 Energy resolution for 40 MeV gamma

For simply getting information on the event depth, z-coordinate of the first conversion point, a variable is introduced into the analysis, which is called here σ^2. The definition of this variable is

$$\sigma^2 = \frac{\sum n_{pe}(i)x(i)^2 + n_{pe}(i)y(i)^2}{\sum n_{pe}(i)} - (\frac{\sum n_{pe}(i)x(i) + n_{pe}(i)y(i)}{\sum n_{pe}(i)})^2 \qquad (4)$$

where $n_{pe}(i)$ is the observed number of photoelectrons in each PMT on the front wall, $x(i)$ and $y(i)$ are the positions of the PMT. The summation is taken for the PMTs on the front face. This variable expresses the broadness of the event shape observed in the front face PMTs, which is related to the depth of the events as predicted by MC simulation shown in Figure 28.

Figure 29 shows the correlation between the N_{pe} and σ^2, and a spectrum of the total number of photoelectrons in the region of $50 \leq \sigma^2 \leq 55$ for the events of the gamma injection at the center of the detector. It can be clearly seen that there is a strong correlation between these two variables. This suggests that the absorption of the scintillation light in liquid xenon is larger than our expectation. The FWHM of the N_{pe} spectrum, evaluated to be 34.8%, deteriorates under this condition due to small photoelectron statistics and the strong correlation.

For understanding what deteriorates the resolution, MC study was done with various input parameters. Results with several λ_{abs} values are summarized in

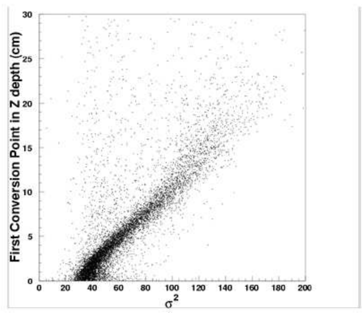

Figure 28: Correlation between depth of the first conversion point and σ^2 predicted by MC.

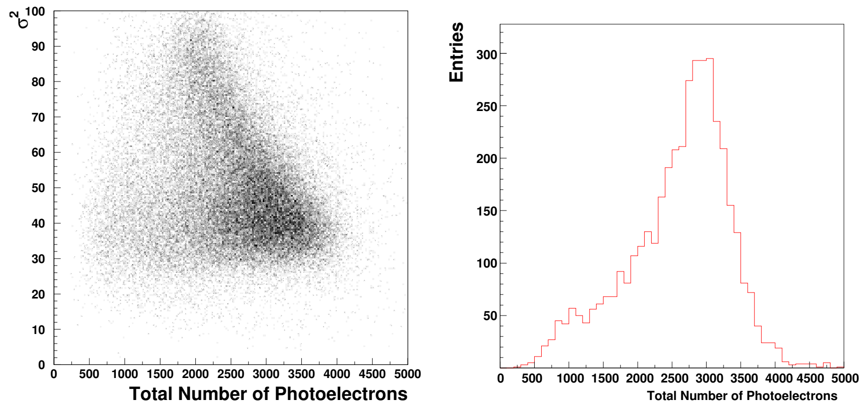

Figure 29: Correlation between N_{pe} and σ^2 (left) and N_{pe} spectrum in the region of $50 \leq \sigma^2 \leq 55$ for 40 MeV compton gammas (right).

Table 5. The contribution of the compton-gamma energy spread is estimated to be 6.11%(FWHM) in case of no scintillation light absorption. The effect of calibration accuracy of the PMTs is estimated, most conservatively, to be less than 2.6%(FWHM) if we consider the quantum efficiency distribution in Figure 26 is unknown. The obtained FWHM can be explained with a short λ_{abs} around 7 cm and the other effect are negligibly small in this condition. Figure 30 shows Monte Carlo prediction for the correlation between N_{pe} and σ^2. It assumes the Rayleigh scattering length (λ_{Ray}) is 30 cm and λ_{abs} is 7 cm (top left), 100 cm (top right), and 500 cm (bottom). The dependence shown in Figure 29 is reproduced fairly well although there is a discrepancy in low σ^2 region due to incomplete modelling of MC.

Table 5: Input parameters of λ_{abs} and expected FWHMs with each input. The FWHMs were estimated using 40 MeV monochromatic gammas.

Absorption length (λ_{abs})	FWHM
7 cm	35.72%
10 cm	22.33%
50 cm	4.23%
100 cm	1.93%

8.1.5 Position resolution

For determining the gamma incident position, it is important to define the size of an event so that the reconstruction should be affected as low as possible by shower fluctuations. For this reason the gamma incident position is reconstructed in 2 steps as described below. The first step is to find a peak position of the light distribution. The second one is to determine more precisely the incident position by an iteration process. A region is selected around the predetermined peak and the weighted mean of the distribution is calculated, where the region size is optimized with MC simulation so that we can get the best position resolution. The mean value is set as a new peak position value and the interaction is repeated until the peak position converges. Position reconstruction for x- and y-coordinates were done independently using a common algorithm. The algorithm uses information only from the front face PMTs arranged in a 6×6 matrix.

Figure 31 shows distributions of reconstructed positions for 40 MeV compton gammas incident on 4 different positions[3]. MC predictions are also shown in Figure 32. It can be seen that data is slightly worse than MC prediction in which the λ_{abs} of 10cm is taken into account. Reconstructed y-coordinate has a similar distribution. Note that in this analysis the effect of beam spread is not subtracted though that is expected to be small enough.

Figure 34 shows a comparison of data to MC simulations with different λ_{abs}'s. The horizontal axis shows distance between the gamma incident position and the nearest PMT center. It can be seen that the obtained resolution can be explained by introducing a λ_{abs} around 7 cm into the simulation and that we

[3]The gamma incident positions are explained in Figure 33

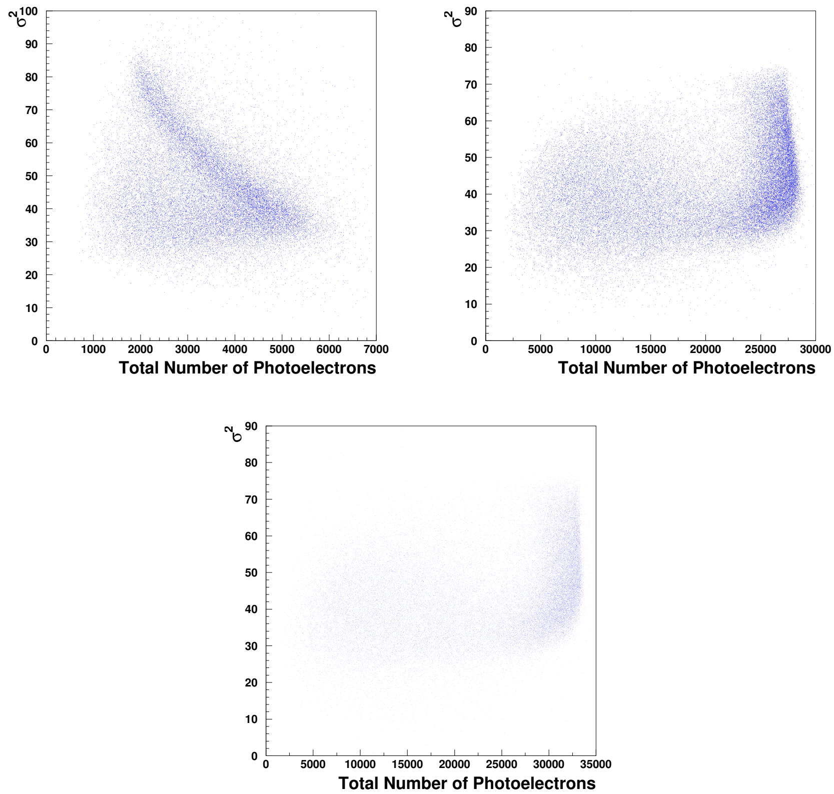

Figure 30: Monte Carlo predictions for the correlation between N_{pe} and σ^2. λ_{Ray}=30 cm and λ_{abs}=7 cm (top left), 100 cm (top right), and 500 cm (bottom) are assumed in the simulation.

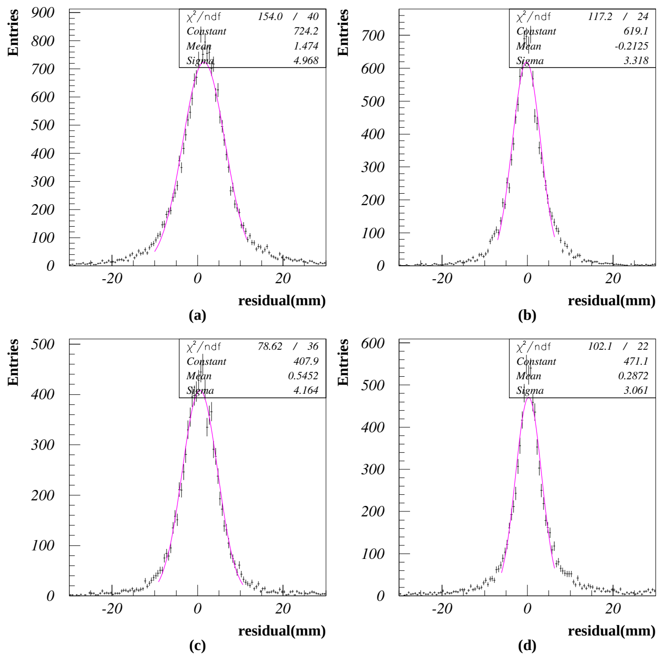

Figure 31: Distribution of reconstructed position for 4 different gamma incident positions for 40 MeV compton gammas. The gamma incident positions (from (a) to (d)) are explained in Figure 33.

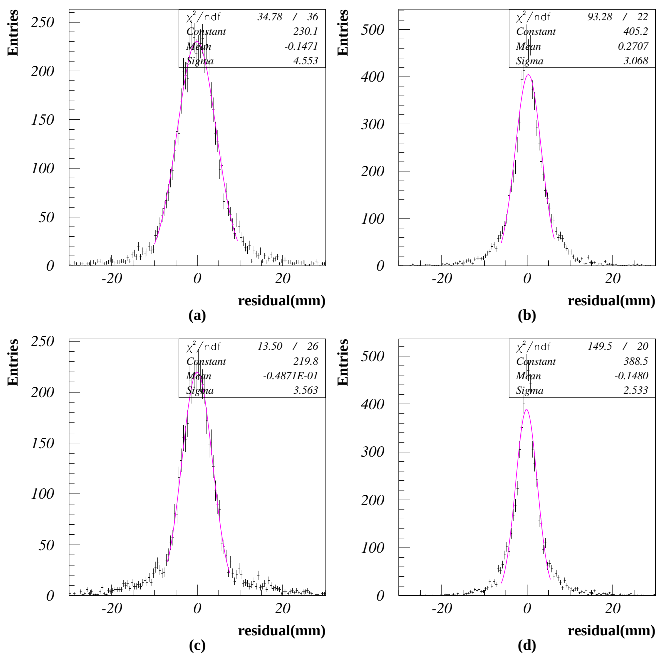

Figure 32: MC predictions of reconstructed position distribution for 4 different gamma incident positions. The gamma incident positions (from (a) to (d)) are explained in Figure 33.

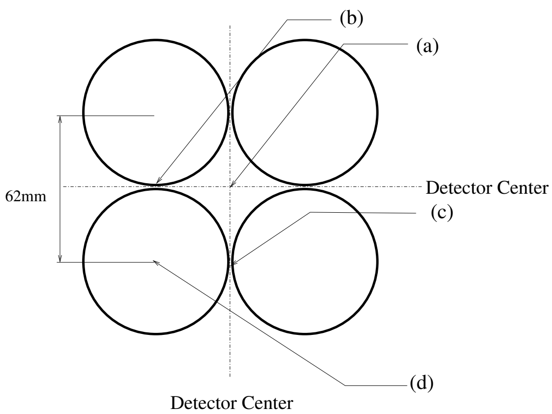

Figure 33: Gamma incident positions on the front face PMTs for position resolution study.

can improve position resolution when we achieve a sufficiently long λ_{abs} of the order of 1m, especially for events incident on the center of adjacent PMTs.

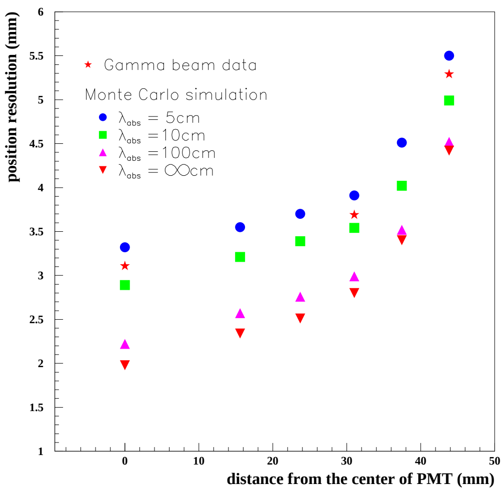

Figure 34: Comparison of position reconstruction resolution (in σ) between data and MC with several kinds of λ_{abs}'s as input parameters.

8.2 Purification system

8.2.1 Mass spectrometer analysis

After the beam test, the detector was moved from AIST to KEK for studying more carefully the impurity problem. A quadrupole mass spectrometer was introduced as a device for remaining gas analysis (RGA) to investigate what kind of material exists in the chamber before filling xenon. The chamber was evacuated again at KEK for RGA. A part of the remaining gas in the chamber during evacuation (2.0×10^{-2} Pa) was sampled to the analyzing section (1.0×10^{-3} Pa). Figure 35 shows the mass spectrum of the remaining gas. Several peaks corresponding to helium(mass number=4), water(18), nitrogen(28), oxygen(32), CO_2(44) can be seen. The peak existing around the mass number of 65 corresponds to xenon whose electron was stripped additionally. Consequently xenon was observed as a molecule with half of xenon mass number (131). Among these peaks it is clearly seen that water contamination is the biggest one and dominates the reached vacuum level.

8.2.2 System description

For removing water contamination that could remain even after evacuation by a turbo pump, a new gas system was added to the gas system for circulating and purifying xenon during detector operation with a heated getter gas purifier. This purifier employs metal getter technology based on zirconium metals that form irreversible chemical bonds to remove all oxide, carbide and nitride impurities

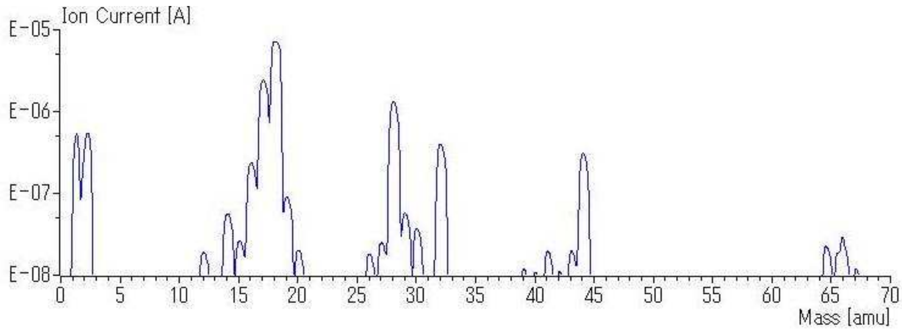

Figure 35: Mass spectrum of the remaining gas.

down to the level of ppb. The purifier can handle the gas flow rate up to 30 liters/minute. A 0.003 micron metal filter is also equipped in this purifier to remove dust particles that could absorb ultra violet light. Figure 36 shows a circulation system schematically. Xenon evaporates around the liquid surface and is transferred to the purifier through a diaflam circulation pump. Then almost all kind of impurity in xenon gas is removed by the purifier. After that the purified gas is returned and liquefied in the chamber. The circulation rate is 10-12 cc/minute in liquid, which is currently limited by the power of the circulation pump. More cooling power is required during circulation for liquefying returned xenon gas in addition to the power for recondensation of evaporating xenon in the chamber. The required additional cooling power is calculated to be 55W for this flow rate, which is overload for the refrigerator currently used. For this reason the detector operating condition during circulation is different from that of refrigerator alone operation. The pressure in the chamber changes from 0.13MPa to 0.135MPa depending on the liquid nitrogen flow though this does not cause any problem for scintillation light measurement.

8.2.3 Performance of the purification

Purification test was performed after RGA. Firstly 120 liters of xenon was liquefied and the stable detector operating condition was established. After that the purification cycle was started with passing xenon from the chamber through the purifier, and liquefying it again in the chamber. Immediately after purification was started, the light yield started to increase both for cosmic-ray and alpha events. In Figure 37 (left) is shown the light yield transition for alpha events of PMTs located at 7.6cm and 11.6cm away from alpha sources. It is also shown in Figure 37 (right) how N_{pe} increases for cosmic-ray events as a function of time. In this case the path lengths of scintillation light to the PMTs is longer than the case of alpha events, so the light yield increases more steeply.

Purification cycle can be modeled like followings; Variation of impurity contamination should be proportional to the impurity density at that time if there is no more outgassing contamination at low temperature. So the impurity density in the chamber can be expressed as a function of time:

$$C(t) = C_0 exp(-\frac{t}{\tau}) \tag{5}$$

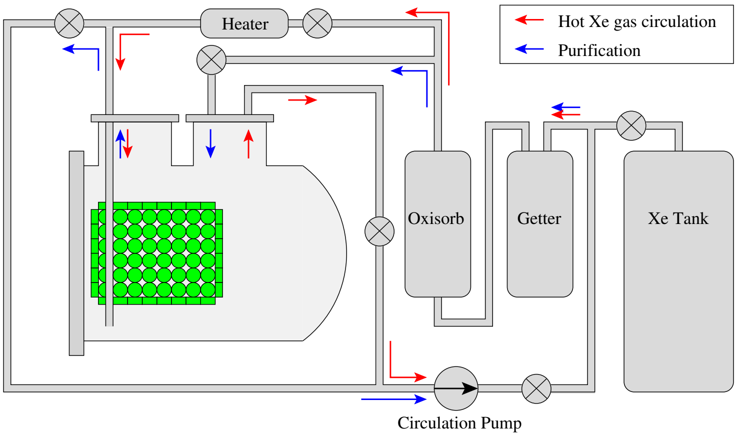

Figure 36: Diagram of the circulation system. Gas flow is indicated with arrows. Two kinds of gas circulation mode are prepared. One for purification and the other for hot gas circulation to warm up the detector. Hot gas circulation is under investigation to remove impurity contamination effectively before starting liquefaction.

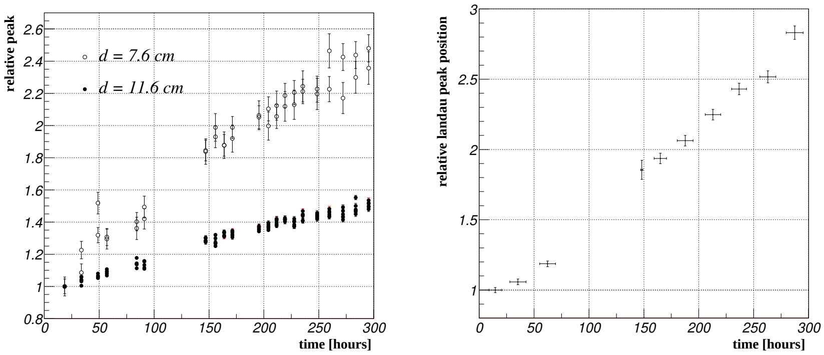

Figure 37: Light yield transition for alpha events observed by PMTs located at 7.6cm and 11.6cm away from alpha sources (left). For cosmic-ray events is shown in (right).

where C_0 is the initial value of the impurity density in the chamber and τ is the time constant of the purification cycle, which is determined by the purification speed and efficiency. The length of absorption caused by this impurity is written with the same time constant as:

$$\lambda(t) = \lambda_0 exp(\frac{t}{\tau}) \tag{6}$$

where λ_0 means the initial value of the absorption length. So the number of photoelectrons observed by PMT(s) at an effective distance of r from the light emission point is written as:

$$N(r,t) = N_\infty exp(\frac{r}{\lambda_0} exp(\frac{t}{\tau})) \tag{7}$$

Light yield transition for cosmic-ray events shown in Figure 37 is fitted with this function. The obtained time constant (τ) is 356.8±11.63 hours. A similar analysis was made for alpha events and we obtained a consistent result of the time constant, that is ~350 hours.

We have been circulating and purifying xenon continuously for more than 40 days. We made various kinds of tests during these days to understand the purification process by stopping purification, stopping circulation, increasing the flow rate and so on. Figure 38 shows the distribution of N_{pe} after 600 hours purification. The light yield for cosmic-ray events has increased by more than factor of 4 compared to the yield at the start of purification.

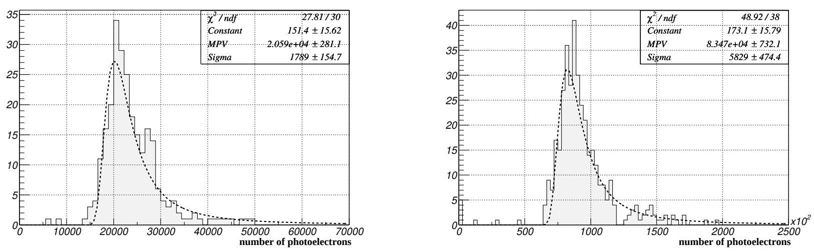

Figure 38: Distribution of N_{pe} for cosmic-ray events triggered by the middle trigger counter set. Before purification (left) and after 600 hours purification(right).

8.2.4 Future prospect

Further study will be done in this summer for optimizing the purification process. It is important to study how we can increase the purification speed. In this study followings things are to be investigated;

1. Study on the material used in the prototype,
2. Possible method of baking the material during evacuation, and
3. Increasing flow rate of the purification.

It is considered to replace plastic material in the chamber to metal or to Teflon so that we can reduce amount of remaining water as much as possible before starting liquefaction. We also plan to raise the temperature of the detector while evacuation so that sticked water molecule can easily escape from the material surface. However, because PMTs are included in our detector that should not be heated above 60°C, care must be taken when warming the detector not to make big temperature gradient in the chamber. For this purpose we plan to circulate hot nitrogen gas after rough evacuation. The chamber will be evacuated again after nitrogen circulation until the vacuum level will reach to the sufficient level. Increasing the flow rate of the purification is also an important issue. If we can handle higher flow rate, we can reduce time to be invested for xenon purification.

8.3 Estimation of the absorption length

8.3.1 Absorption length during the gamma beam test

As described above, the deterioration of the detector resolutions, especially energy resolution, is attributed to a shorter λ_{abs} of the scintillation light under the detector operating condition during the beam time. We estimated the λ_{abs} by using cosmic-ray and alpha events collected during the gamma beam test. Details of the analysis are summarized in a separate note [16]. Figure 39 shows the number of photoelectrons observed in the front (or back) face PMTs as a function of reconstructed z-coordinate of cosmic rays. The reconstruction was done by using the N_{pe} information from PMTs belonging to the different detector faces. MC predictions with different λ_{abs}'s (5cm, 10cm, 50cm, and 100cm) are superimposed. In the MC simulations λ_{Ray} was supposed to be 30cm [17]. There are discrepancy in shape between the data and MC: the data distribution is steeper near the face and falls less violently for large z. This discrepancy can be explained by introducing wavelength-dependent absorption effect by some impurity such as water into the MC (Figure 40): some light is readily extinguished after a few cm, while a surviving component (a few percent) exhibits a longer (of the order of one meter) λ_{abs}. Alpha events were also analyzed to estimate

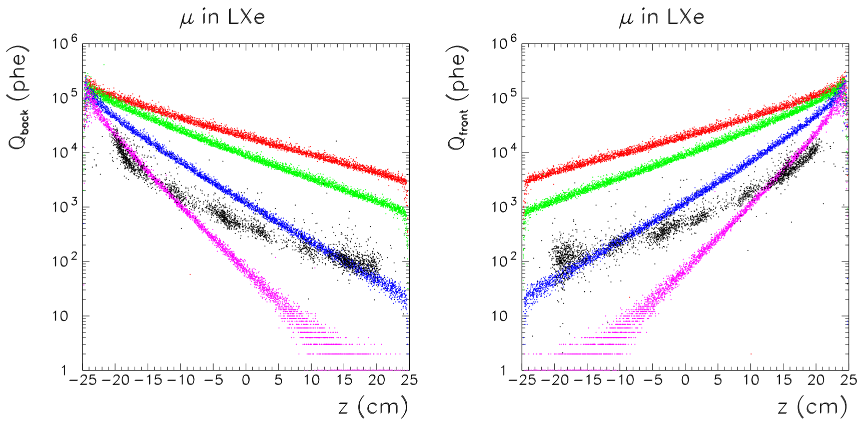

Figure 39: Number of photoelectrons observed by PMTs on the back and front faces for cosmic events.

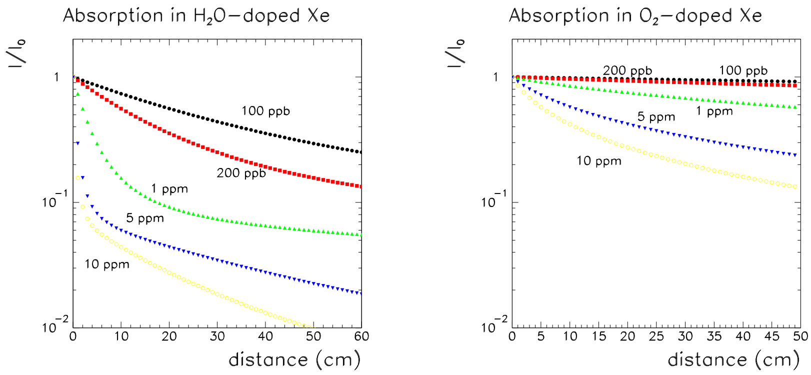

Figure 40: Simulation of the light absorption by water and O_2 for different level of contamination.

the λ_{abs}. Figure 41 (left) shows the ratio of observed number of photoelectron to the MC prediction with input parameters of λ_{abs}=∞ and λ_{Ray}=30cm as a function of the distance from alpha sources to PMTs. In Figure 41 (right) is shown a same distribution but with different input parameters of λ_{abs}=7cm and λ_{Ray}=30cm. It can be seen that the distribution is consistent to be 1 around the short distance region, while PMTs located at more than 30cm away from the source seem to receive more light than predicted. This is the same feature as seen in the cosmic-ray event analysis that is reasonably explained by a wavelength-dependent absorption by impurity.

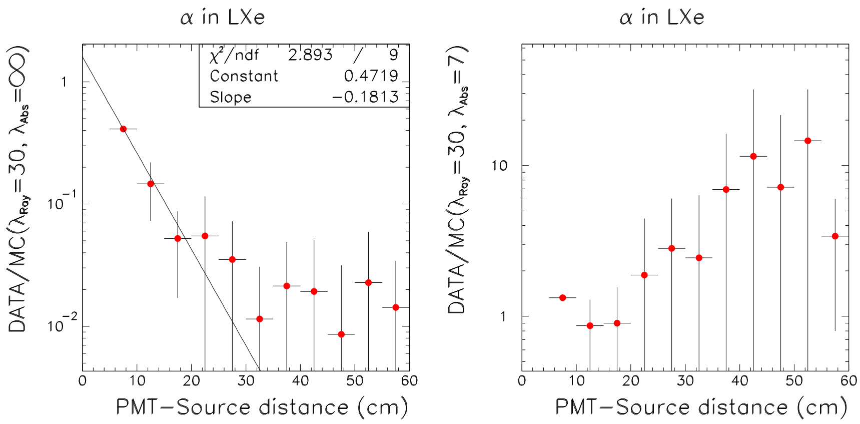

Figure 41: Ratio of N_{pe} for alpha events to MC prediction as a function of the distance between alpha sources and PMTs.

In conclusion it is certain that there was impurity contamination during the detector operation for the gamma beam test. Cosmic-ray and alpha data taken during the beam test indicate a short λ_{abs} less than 10 cm in liquid xenon.

8.3.2 Absorption length after purification

Absorption length was estimated also after starting the purification using the similar method as described above. Figure 42 shows the comparisons of alpha data in liquid xenon to MC (left) and to alpha data in cold gas (right)[4]. Three different sets are shown for data before purification (circles), after two weeks purification (squares) , and after one month purification(stars). In the MC simulation employed here we used λ_{Ray}=45 cm which is evaluated using our recent data after purification instead of 30 cm. The evaluation was done by comparing the number of photoelectrons observed by PMTs on the same surface of the alpha source to the MC predictions. The value of λ_{Ray}=45cm is in agreement with recent calculations [18]. The figure shows apparent growth of the absorption length thanks to purification. However it is clear that the 2nd and 3rd data points are always located below other points. The corresponding PMTs to these points are located on the front face and see the alpha sources with large angles. In addition their signals are read by consecutive electronics channels which might have experienced some problems. Further investigation is required for complete understanding of the data.

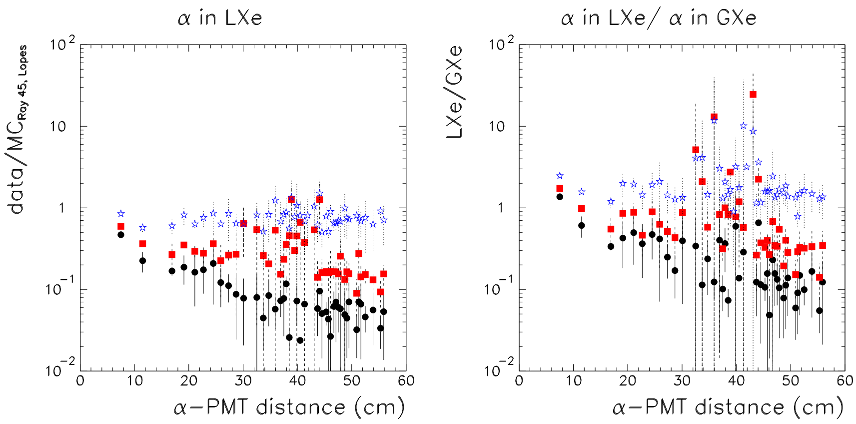

Figure 42: Comparison of alpha data in liquid xenon to MC (left) and to alpha data in cold gas xenon (right) for three different runs: before the purification (circles), after two weeks purification (squares), and after one month purification (stars).

In order to estimate λ_{abs}, the newest data (shown in starts in Figure 42) was re-histgramed and fitted with exponential functions. The 2nd and 3rd points in Figure 42 were excluded in fitting. The results are shown in Figure 43. From the comparison with the gas data, we can evaluate an effective λ_{abs} of 80 cm, which however includes the effect of scattering only in liquid data and therefore represents a lower limit of the λ_{abs}. The exponential fit to the comparison with MC, which include the effect of Rayleigh scattering (λ_{Ray}=45 cm), does not show a significant slope. We can therefore use the result to establish a lower limit of 100 cm at 95% confidence level for the λ_{abs}.

[4]Because absorption and scattering in gas xenon influences light transportation less than in liquid xenon, the gas xenon data was taken as a reference.

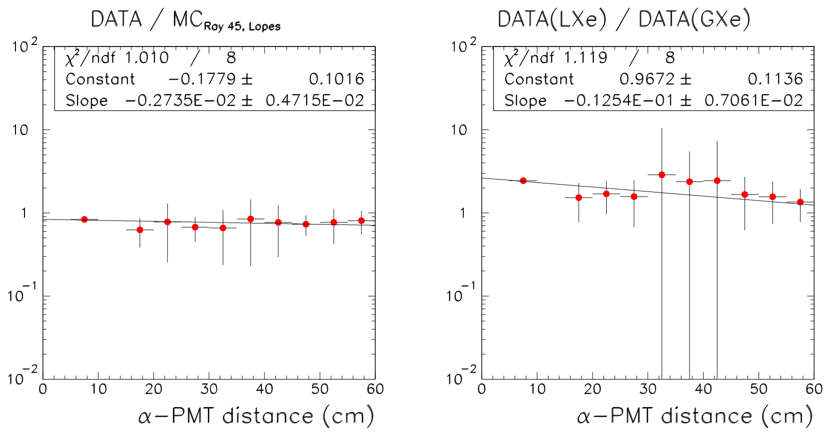

Figure 43: Absorption length determination from the comparison to MC(left) and to the cold gas data(right).

We compared also the cosmic-ray data to the MC predictions using the observed number of photoelectrons. In this case the comparison is more dependent on the parameters in the MC such as the W value (required energy for emitting one scintillation photon) and on the modeling such as reflection of light on the PMT windows, however, we can conclude that the observed light yield agrees with our MC prediction which includes the λ_{abs} of 100 cm. This means that predicted performance by our MC with λ_{abs}=100cm is confidently achievable.

8.4 PMT development

PMT development has been continued in collaboration with Hamamatsu Photonics. The previous PMT uses a manganese layer between the silica window and photocathode as a conductive layer for preserving the surface electrical conductivity of the photocathode at low temperature. However it was pointed that this layer could absorb the scintillation light, resulting in lower quantum efficiency. As a replacement of the manganese layer, a new aluminum grid is designed as shown in Figure 44.

Although the area covered with the aluminum is insensitive to light, it is expected that we can increase quantum efficiency in total of sensitive photocathode area by removing the manganese layer. A sample of the new PMT was made and the quantum efficiency was measured for ultra violet light below 200nm at room temperature. The measured value is 14.5% at 175nm, which is more than 2 times larger than that of the previous PMT. Test at low temperature was performed using a simple setup with low temperature gas xenon shown in Figure 45. An ^{241}Am alpha source was placed to induce scintillation light in gas xenon and two LEDs were located for PMT calibration. Figure 46 shows the distribution of N_{pe} spectra of the new and previous PMTs for alpha events in low temperature gas xenon. It can be seen that the output of the new PMT is larger by factor of 3 similarly at room temperature.
It is important to study the rate dependence of the new PMT output for high

Figure 44: New PMT with an aluminum grid under the photocathode.

rate operation in the muegamma experiment and to test the PMT response with sufficient amount of samples. However the new PMT uses the same dynode structure, the same metal tube, and the same bleeder circuit, thus basic characters of the PMT such as tolerance to the magnetic field and pressure, and output pulse shape should be same as those of the previous PMT. In addition the thickness of the manganese layer used in the previous model could not be controlled so accurately while the new PMT does not have such uncontrollable process, resulting in PMT production in more constant quality. Further study will be done in this summer.

8.5 Refrigerator development

As reported in the previous report, we are developing a u-shape pulse tube refrigerator for the final photon detector. It is expected to be able to increase the cooling power by employing another configuration of the pulse tube. In the u-shape pulse tube configuration the cold part is well separated from the warm part, resulting in more efficient cooling. A prototype of the u-shape pulse tube refrigerator was constructed in KEK as shown in Figure 47. Two stainless pipes with 42 mm o.d. and 180 mm in length are used for the regenerator and pulse tube. Cooling power of the refrigerator was measured at different temperature as presented in Figure 48. Comparison between the cooling powers of coaxial and u-shape refrigerators is also shown. Even with smaller compressor power, the u-shape refrigerator has a similar COP (Coefficient Of Performance) in this preliminary measurement.

8.6 Final photon detector

8.6.1 Expected Performance

In this section, based on the present knowledge obtained from the studies with the prototype detector, the expected performance of the final photon detector is evaluated using the MC simulations.

As is clear from the preceding sections, the detector performance depends

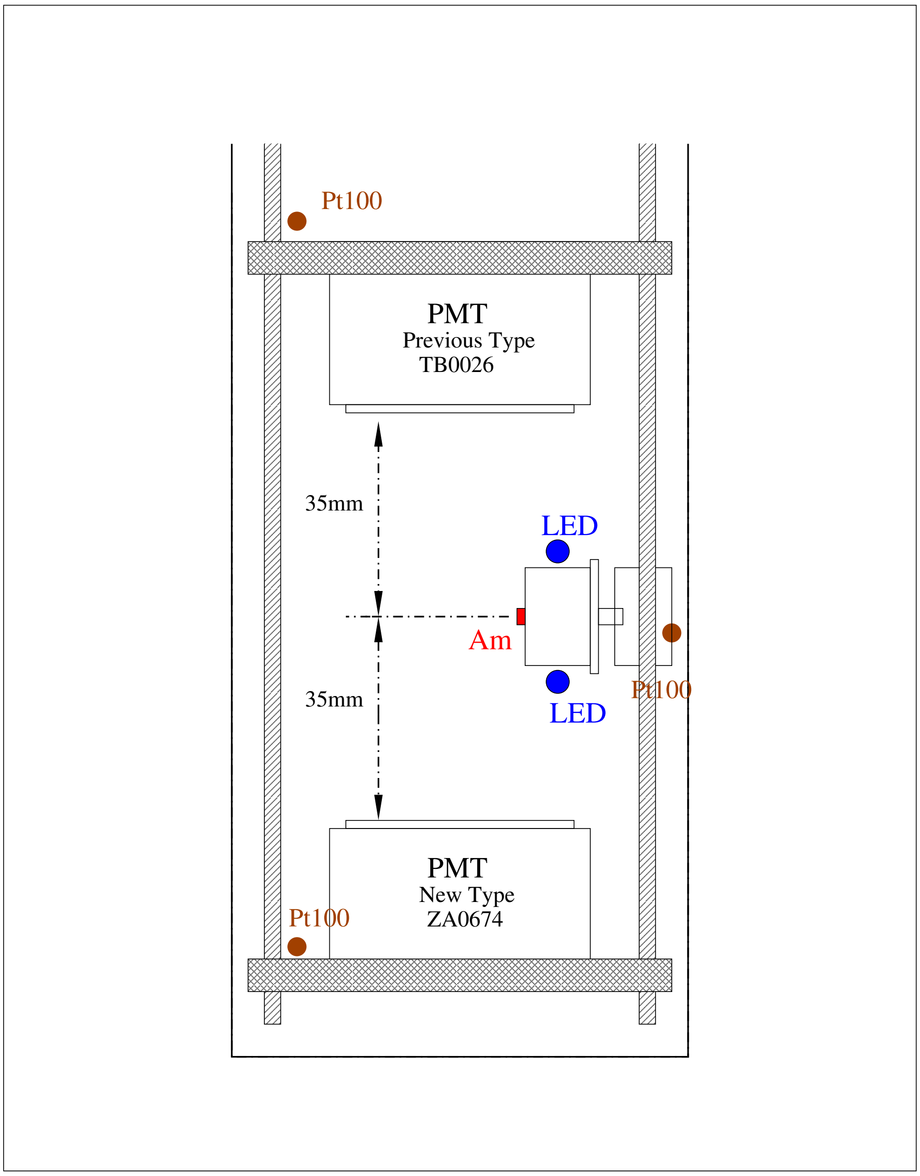

Figure 45: Schematic view of the new PMT test setup.

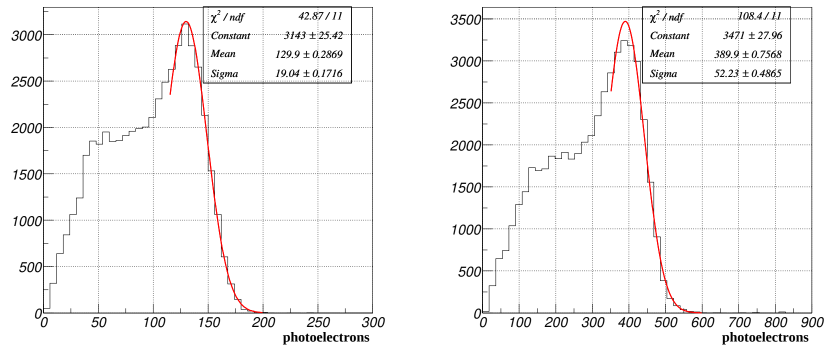

Figure 46: Distributions of N_{pe} observed with a previous PMT (left) and a new aluminum grid PMT (right).

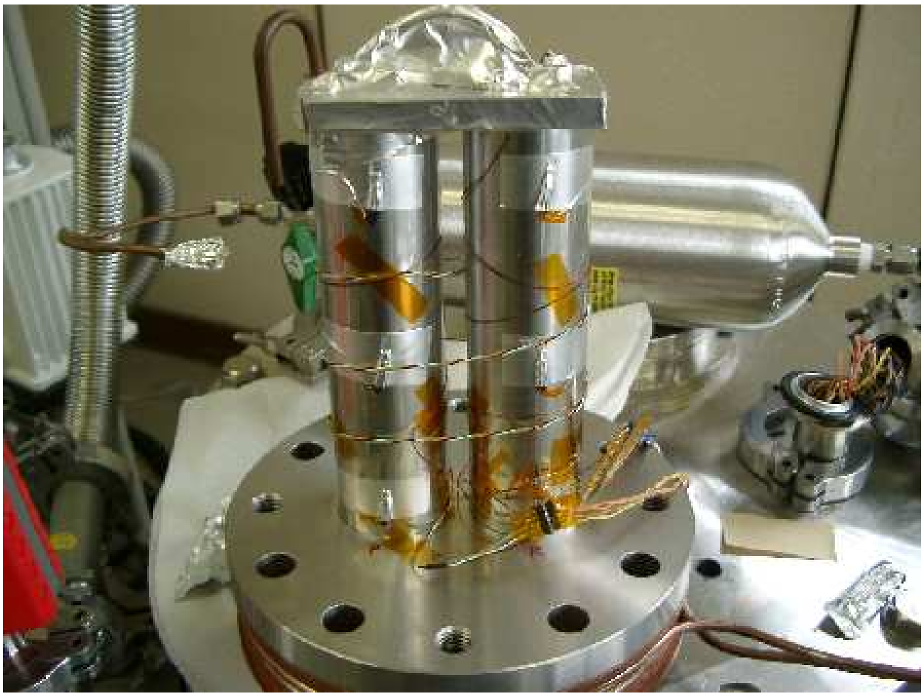

Figure 47: U-shape pulse tube refrigerator constructed in KEK.

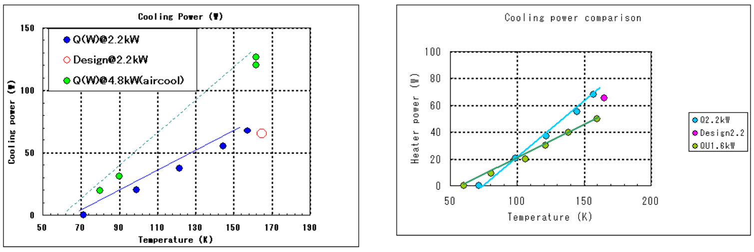

Figure 48: Cooling power of the new u-shape pulse tube refrigerator operated by 2.2kW and 4.8kW compressors(left). Cooling power comparison between a coaxial type operated by a 2.2kW compressor and a u-shape operated by a 1.6kW compressor(right).

largely on purity of xenon which affects the absorption length of the scintillation light. Here we conservatively assume an absorption length of 100 cm we have so far attained with the prototype, although we aim to realize a much longer absorption length in the final detector.

With the C-shaped detection volume of the final detector, arrangement of PMTs is another important factor which determines the performance. To obtain efficient and uniform responses to incident gamma-rays, various arrangements are currently being studied to optimize the performance. However we use a simple, realistic, but still not optimized, arrangement of PMTs for an evaluation here; therefore the performance could be improved with other arrangements in the future. In the configuration studied here, the PMTs are placed as dense as possible at the front (entrance) wall, just like the prototype, with 24 PMTs along ϕ and 13 PMTs along the muon beam direction (z), while the other walls have less dense PMTs (the rear wall: $27(\phi) \times 8(z)$, the up-/down-stream walls: $24(\phi) \times 5(r)$, and the top/bottom walls: $8(z) \times 5(r)$).

Detector resolution

As described in Section 8.1.5, the incident positions of gamma rays can be determined using several PMTs near the incident positions. Therefore the position resolutions in the final detector are more or less the same as those of the prototype, as long as the PMT densities on the front wall are similar. The resolutions obtained from the gamma-ray beam test agree well with those in the MC simulations assuming a 5–10 cm absorption length. With a 100 cm absorption length, the simulation study indicates that the same reconstruction algorithm used for the prototype yields a position-dependent resolution of 5.5–11 mm (9 mm on average, all in FWHM). Another algorithm giving a more uniform response achieves a resolution of 10.6 mm (FWHM). The study also shows that the resolutions slightly improve with higher photo-electron statistics for a longer absorption length.

The conversion position resolution along the "depth" direction was also obtained as 16–18 mm (FWHM) by the simulations. This will have to be verified experimentally later by measuring the timing resolution of gamma rays with the prototype.

For energy measurements, because the density of PMTs is not uniform, the energy of the gamma ray is approximately written as a weighted sum of the charge seen by each PMT Q_i:

$$E = c + \sum_i c_i Q_i$$

The coefficients c_i could be estimated by the so-called "principal components analysis" method [19]. Roughly, in this method the variation of E, σ_E, is evaluated from the covariance σ_{ij} of Q_i:

$$\sigma_E 2 = \sum_{i,j} \sigma_{ij} c_i c_j$$

The covariance matrix σ_{ij} is calculated from the simulated events of interest, 52.8 MeV gamma ray events in this case, and the coefficients are determined to minimize $\sigma_E 2$.

Assuming a 1 m absorption length, this method yields an average of 5 % (FWHM) resolution (Fig. 49) for gamma rays uniformly entering the detector with energy of about 50 MeV. We can further improve the resolution by exploiting the knowledge of the photon conversion point: if we prepare different sets of the coefficients c_i for different incident positions by bins of 5×5 cm^2, it improves to 4 % (FWHM).

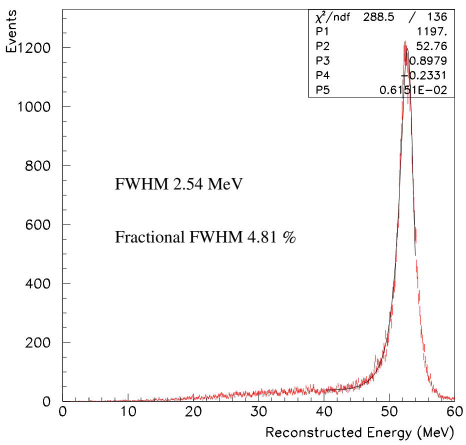

Figure 49: Reconstructed energy distribution for photons from $\mu^+ \to e^+\gamma$.

Photon detection efficiency

As the designs of the COBRA magnet, the PMTs, and the entrance window of the photon detector, are being finalized, the effects of the interactions in the front materials and the energy leakage from the front wall are re-evaluated by the MC simulations.

The result is shown in Fig. 50. With ±4 % energy cut, the detection efficiency is 74 %. There is no observable degradation in the energy resolution.

The efficiency for reconstructing gamma rays is not yet known, as the reconstruction algorithms are still being optimized. A possible inefficiency may result from gamma ray conversions very close to the PMT surface. The algorithms currently under development try to reconstruct the gamma rays even in such cases but with poorer resolutions. A very crude estimate might be that we could lose all the events where the conversion occurs within 1 cm from the PMT surface that amount to about 15 % of the events, leading to about 85 % reconstruction efficiency.

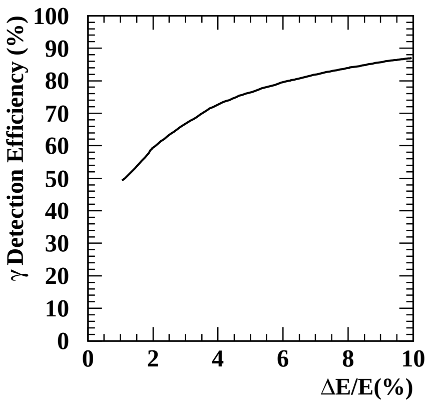

Figure 50: Detection efficiency of a 52.8 MeV γ ray as a function of half width of energy cut ($\pm\Delta E_{\gamma}$).

8.6.2 Calibration method

Calibration of the PMTs in the final photon detector will be done by using in priciple the same method employed in the large prototype study. All PMTs will be inspected before installation by measuring amprification gain and quantum efficiency at around the operating voltage. Gain of the PMTs will be continuously monitored and adjusted by using LEDs periodically during the experiment. Relative estimate of effective quantum efficiency, which includes the collection efficiency of the phtoelectrons to the 1st dynode, under the existence of magnetic field is as important as the periodical gain calibration of the PMTs. For this purpose, as demonstrated in the large prototype study, scintillation light induced by alpha particles in cold gas xenon is available because the absoprtion and scattering effects are small enough that we can well simulate the light transmission. Configuration of the alpha point souces has to be optimized while designing PMT configuration on the lateral and back faces.

It is planned to use π^0 decays to $\gamma\gamma$ for absolute energy calibraion and for evaluating the detector resolution. The timing resulution will be improved and evaluated as well as that of the positron timing counter using radiative muon decays.

8.6.3 Cryostat design

Design of the cryostat and cryogenics controlling system has been considered based on the experiences obtained with the large prototype.

Mechanical calculation of the cryostat was completed using a finite element analysis method. We have almost finished the drawing work of the cryostat. Details of the construction and detector installation procedure are now discussed. Design work of the cryogenics scheme and controlling system has been also started. Circulation and purification scheme is included in this design. Figure 51 shows a preliminary design of the cryogenics system. Detailed examination of the controlling system is now advanced.

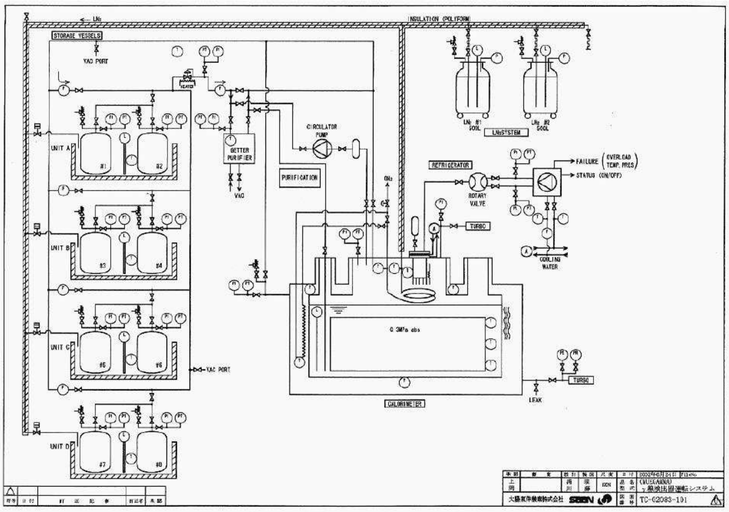

Figure 51: Design of the cryogenics system.

In the experiment xenon will be stored in 8 tanks of 285 liters volume each of which can keep xenon of 420 kg corresponding to 140 liters in liquid at 165 K. Two of the 8 tanks had been used in the large prototype studies for xenon storage. Recovery of xenon after a test is done by cooling the tank(s) with liquid nitrogen. Liquefaction and recovery has been repeated 7 times during the large prototype study without any problem. For the final detector operation and maintenance storage and recovery will be done in the same manner. However it is also important to consider how to recover xenon in case of emergency, for example break of vacuum for the thermal insulation. During the detector operation, for this purpose, remaining xenon gas in the tanks will be transferred to one tank and the other 7 tanks will be kept in vacuum. If it would be necessary to recover all xenon immediately due to unwanted trouble, firstly xenon would be recovered to the 7 tanks that act as 2000 liter buffer. During this recovery to the buffer, the remaining tank will be cooled with liquid nitrogen and start to store up xenon.

We plan to start construction of the cryostat in this year. It will take 4 months for construction. Low temperature test and heat load measurement will be done soon after construction. Liquefaction test using 800 liter xenon will be performed before installing PMTs. The control system and refrigerator should be ready prior to this test together with the storage and recovery system of xenon.

9 Trigger, Electronics and DAQ

9.1 Slow Control System

Particle physics experiments require what is commonly referred to as "slow control". This includes the measurement and control of environment variables such as temperature, pressure and humidity as well as the control of high voltages for photomultipliers and wire chambers. While most experiment use an inhomogeneous mix of systems involving RS232, GPIB and PLCs, our experiment will use a new slow control system developed at PSI, called MSCB (Midas Slow Control Bus). This system will be used for the 960 high voltage channels of the experiment, for the control of the liquid xenon calorimeter and for the superconducting solenoid. The integration of all these systems into the central data acquisition and control system is essential for the long-term stability of the experiment.

The MSCB system uses a field bus- like architecture, where a number of "nodes" are connected to a serial bus, which is controlled by a central PC. Each node contains ADCs, DACs and digital I/O for measurement and controlling tasks. For critical installations the control PC can be backed up by a secondary PC for redundancy. The PCs are connected to the Midas DAQ system [20], which allows for remote operation through a Web interface, history display, automatic alarm notification and for logging of slow control variables to tape.

The hardware of a MSCB node is designed around a new generation of microcontrollers, which contain a 8051- compatible microcontroller core, ADCs, DACs and digital I/O on a single chip. We currently use the ADuC812 [21] from Analog Devices and the C8051F000 from Cygnal [22]. The nodes are connected via an RS-485 bus running at 384 kBaud. A segment can contain 256 nodes, and with one layer of repeaters 65536 nodes can be connected and addressed on a single bus. Two versions of MSCB nodes have been developed. A stand-alone module (Fig. 52) which can be embedded directly on a sensor or on an electronics board is powered from the bus, which uses a 10-wire twisted pair flat ribbon cable for distances up to 500 m. The production cost of such a node is about 30 USD.

In addition to the stand-alone module, a 19" rack system which hosts cards containing a MSCB node and signal conditioning, has been designed. Cards were made for voltage, current and temperature measurements as well as to control 220V consumers such as heaters. The MSCB bus runs on the back plane of the crate.

Using the local intelligence of the node controller, regulation loops (PID) and interlock systems can be realized without intervention of the central control PC. The nodes run a simple framework for the communication with the host system, which guarantees real-time behaviour. User routines can be added to implement application- specific logic. The nodes can be reprogrammed over the RS-485 bus.

The MSCB protocol was optimised for minimal overhead. A 16-bit value from a node can be read out by sending a request of three bytes and receiving an reply of four bytes, both including a code (CRC) to avoid data corruption. Depending on the number of nodes, a MSCB system can either use 8-bit or 16-bit addressing. A node can contain up to 256 "channels" for reading and writing and up to 256 "configuration parameters", which are stored in the EEPROM

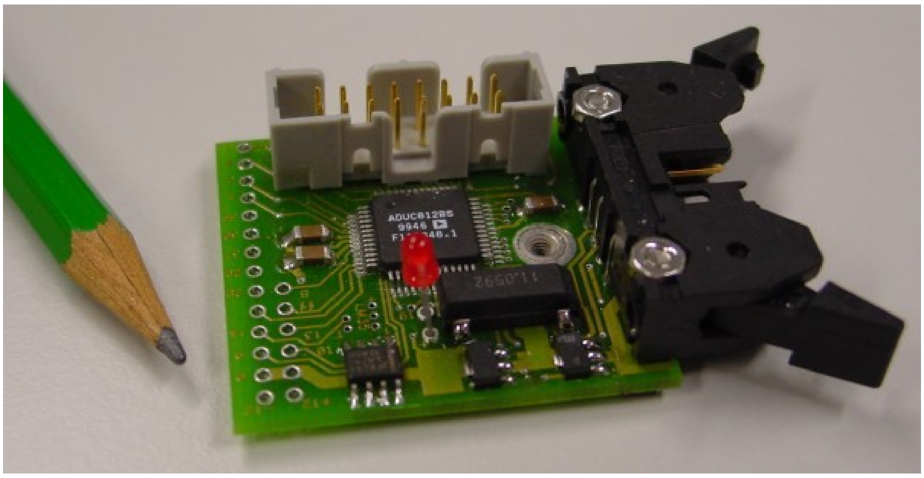

Figure 52: Stand-alone node with an RS-485 transceiver, eight channel 12-bit ADC, two channel 12-bit DAC, 16-bit digital I/O and a temperature sensor. The right connector is for the MSCB bus, the one at the back for an optional LCD display.

of the node and can for example be used as constants for PID regulation. Each channel and parameter is described by a set of attributes such as name, physical units and status. These attributes are stored in each node and can be queried from the control PC, making the configuration of large networks very simple. A special repeat mode has been defined which allows the readout of a series of nodes in less than 300 μs per node.

For the control PC a “C” library has been developed running under Windows and Linux. Based on this library, a LabView driver and a driver for the Midas DAQ system are available. Simple LabView applications such as a data logger with graphical display has been implemented.

A prototype of the MSCB rack system is currently used for the pressure and high voltage control at a different experiment and will soon be adapted for the PSI xenon refilling station. The setup of this system for the control of the photon detector and cobra magnet is under way. For more information visit the MSCB home page at http://midas.psi.ch/mscb.

9.2 High Voltage System

High resolution calorimeters need an excellent stability of the high voltage system. Our 12-stage photomultipliers have a gain variation of about 1% per Volt. Most commercial units have an accuracy of 1-2 Volts over the temperature range seen in the PSI experimental hall. The resulting gain drift from high voltage variations would therefore spoil our energy resolution. We see this effect already at the large prototype where the high voltage stability limits our online gain calibration.

To overcome this problem, a new high voltage system based on the MSCB slow control system has been proposed. An common high voltage is distributed to each channel, which regulates its output between zero and the external voltage. Since each channel contains a MSCB node with a microprocessor, an elaborate self-calibration algorithm using two common high precision reference voltages can be implemented. This, together with a temperature sensor on each channel electronics, ensures a high voltage stability better than $\pm 0.3V$ over the full temperature range of $20\deg C$ to $40\deg C$.

A first prototype with 12 channels has been successfully tested and the full system with 960 channels is now in production.

9.3 Trigger

Detailed simulation studies were performed in order to obtain an estimate of the final acquisition rate expected in the experiment. Background from the accidental coincidence of photons (from the muon radiative decay $\mu^+ \to e^+\nu\overline{\nu}\gamma$ or from positron annihilation in flight) and Michel positrons was considered. A complete GEANT simulation of the proposed experimental set-up was used. We studied the selections based on the photon and positron kinematic variables which could be used in the trigger at various levels.

9.3.1 The photon

The sum of the charge seen by the PMTs of the liquid xenon photon detector can be used by the trigger to obtain an estimate of the photon energy. By setting a threshold equivalent to a 45 MeV photon energy one achieves a $\sim 97\%$ efficiency on the $\mu \to e\,\gamma$ signal while the fraction (per stopped muon) of background photons satisfying this selection criterion is $f_\gamma \simeq 2 \cdot 10^{-4}$. The rate of the calorimeter events satisfying this requirement would result in:

$$R_\gamma = R_\mu f_\gamma \Omega / 4\pi \tag{8}$$

By using a stopping muon rate $R_\mu = 10^8 \mu/\mathrm{s}$ and a solid angle fraction of 10% we would obtain a 2 kHz photon event rate.

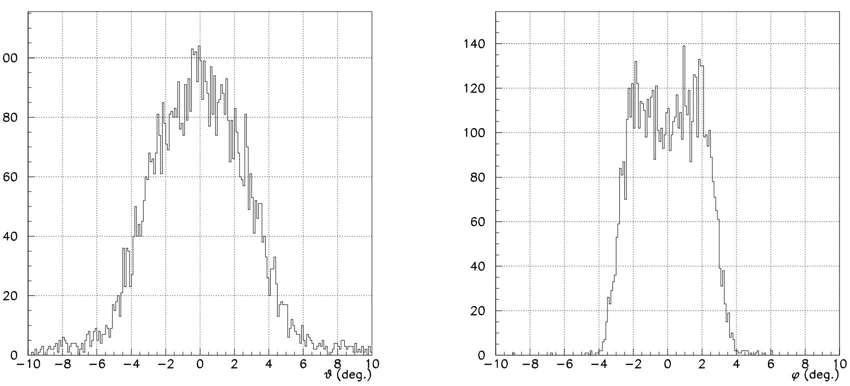

Figure 53: Photon direction determination by means of maximum light PMT. The angles are referred to a coordinate system with the polar axis along the μ beam.

The position of the liquid xenon photon detector inner face PMT which observed the maximum light gives an estimate of the photon direction which is sufficient for trigger purposes. The determination of the photon direction obtained by connecting the maximum pulse height PMT with the center of the target is shown in fig.53 relatively to the true direction.

The scintillation light emission in liquid Xenon has two components and the relative intensity depends on the ionization density of the detected particles. We can define an effective decay time of the ionization light for γ-induced events ($\tau_{\rm eff} \approx$ 22ns). Such a short decay time and the proximity of the photon conversion point to the PMT on the entrance face indicates that the rising edge of the maximum pulse height PMT signal is a good estimator of the γ emission time. The distribution of this variable is shown on the left part of fig.54.

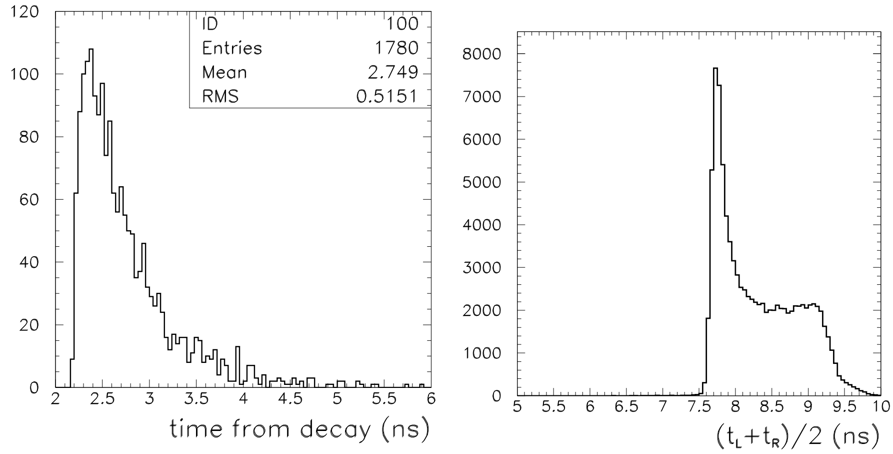

Figure 54: Left: Signal time of the calorimeter PMT with the maximum charge. Right: Positron impact time on the timing counter.

9.3.2 The positron

We estimated that the overall rate in the timing counter due to Michel positrons is $R_{TC} \simeq 5 \times 10^6$Hz .

Each individual scintillator bar of the timing counter is viewed by two PMTs. The average time of the two PMT signal rising edges is a possible estimator of the positron emission time. The distribution of this average time is shown in the right part of fig.54. Without correcting for the positron impact position along the timing counter, the minimal time window, fully efficient on the $\mu \to \mathrm{e}\,\gamma$ event, is $\approx$ 4ns. We are testing the operative definition of the signals timing on real PMT pulses, and we can envisage a safer time coincidence of ΔT = 10ns between a photon and a positron.

The hit patterns on the timing counters, for $\mu \to \mathrm{e}\,\gamma$ events in the angular acceptance range of the calorimeter, can be seen in fig.55. A selection in the photon directions corresponds to a specific region of the timing counter scintillator bars hit by the positron. We found that a 7.5 degree selection in ϕ (coloured bands in fig.55) corresponds to a spread over five out of 20 scintillator bars for the positrons. The efficiency on the $\mu \to e\,\gamma$ signal of this selection is greater than 99.5%. For an accidental background the corresponding rejection factor is $f_\phi \simeq 5$. The equivalent rejection factor in the zenith case is lower ($f_\theta \simeq 2$) due to the target bending along the beam axis.

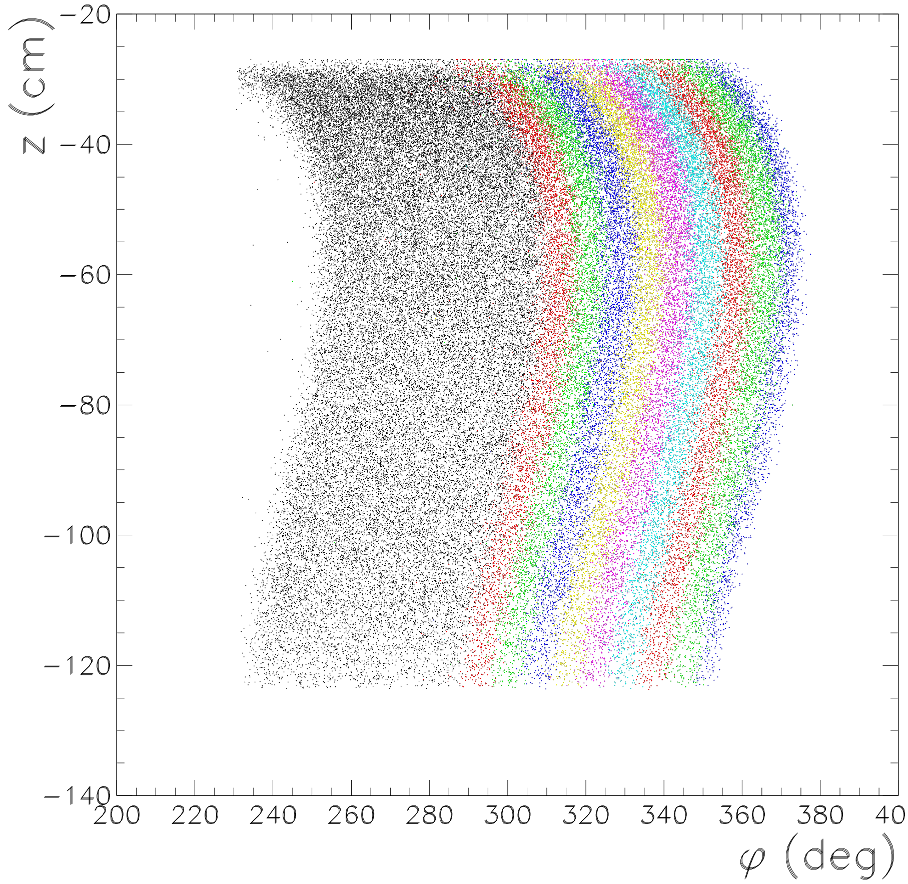

Figure 55: Hit patterns on Timing Counter for $\mu \to e\,\gamma$ positrons in the acceptance angular range. Different coloured bands correspond to 7.5 deg.-wide intervals in ϕ.

As illustrated in the proposal [1], the maximum radius (R_{DC}) reached by a positron in the drift chamber of the COBRA spectrometer is a measurement of its total momentum. For more than 99.5% of the positrons from $\mu \to e\,\gamma$ decays $R_{DC} > 26.5\,\mathrm{cm}$, which corresponds to leaving a signal in one of the last seven wires of a drift chamber of the COBRA spectrometer. We can envisage using the signals from these wires for an additional trigger level. However, a cut on the drift chambers radius does not correspond to a big rejection factor as can be seen from figure56 , where we show the momentum distribution of all the Michel positrons hitting the timing counter (continuous line) and those satisfying the previous condition on R_{DC}. The rejection factor that could be reached in this way is about 2.

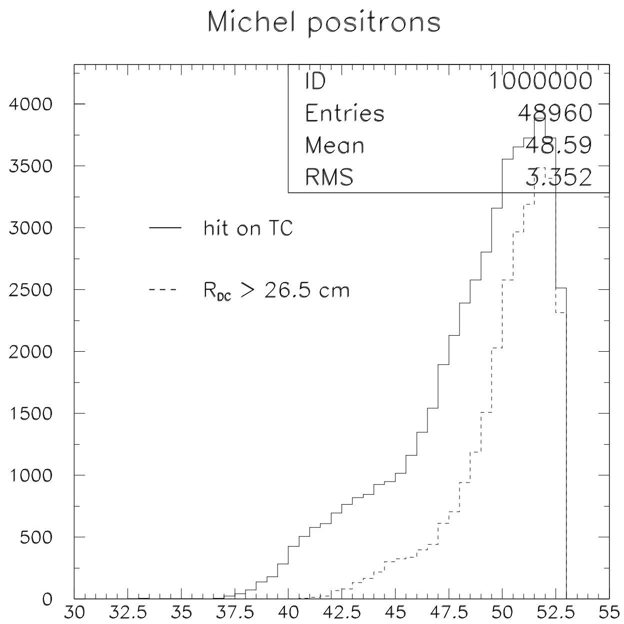

Figure 56: Momentum distribution of Michel positrons hitting the Timing Counter (solid line) and those with $R_{DC} > 26.5$ cm (dashed line).

9.3.3 The trigger rate

We are designing a trigger system that collects signals from the Liquid Xenon Calorimeter and the Timing Counter. The information provided by the Drift Chamber is available with some delay; therefore the Drift Chamber cannot be used for a fast Level 1 trigger.

By requiring at least a 45 MeV energy release in the liquid Xenon the calorimeter event rate is $R_\gamma = 2\,\mathrm{kHz}$ as obtained from equation (8).

The presence of a hit in the Timing Counter, within a time coincidence window of $\Delta T = 10\,\mathrm{ns}$ and spatially aligned with the measured photon direction, reduces the uncorrelated background event rate to

$$R_{L1} = 2 R_\gamma R_{TC} \Delta T \frac{1}{f_\phi f_\theta} \approx 20\,\mathrm{Hz} \tag{9}$$

The estimated trigger rate gives us some margin in case of other possible contributions to the background which are not taken into account in the simulation. Furthermore different algorithms, less conventionals and intuitives, are currently under study. In principle they provide better estimators of the physical quantities and therefore they are less sensitive to other possible sources of background. The trigger system should have the capability of accommodating both algorithm classes.

9.3.4 The trigger system

Both the Liquid Xenon Calorimeter and the Timing Counter are read out by means of PMTs. The large number of analog channels, together with various and complex physical quantities to evaluate, suggest a digital implementation of the reconstruction algorithms. Today's high density Field Programmable Gate Arrays (FPGAs) coupled with fast Flash Analog to Digital Converters (FADCs) are the key elements of the trigger system. The hardware digital approach, coupled with the FPGAs programmability, allows a simple system design and is both extremely powerful and flexible at the same time.

We are currently designing a trigger system based on two different electronics boards only. A first board (Type1) receives and digitizes the PMT signals, pre-processes the digitized waveforms and sends this information, through Low Voltage Differential Signaling (LVDS) connections, to a second board (Type2) which completes the trigger algorithms. Board Type2 communicates with other boards through LVDS connections too. These two types of boards are arranged

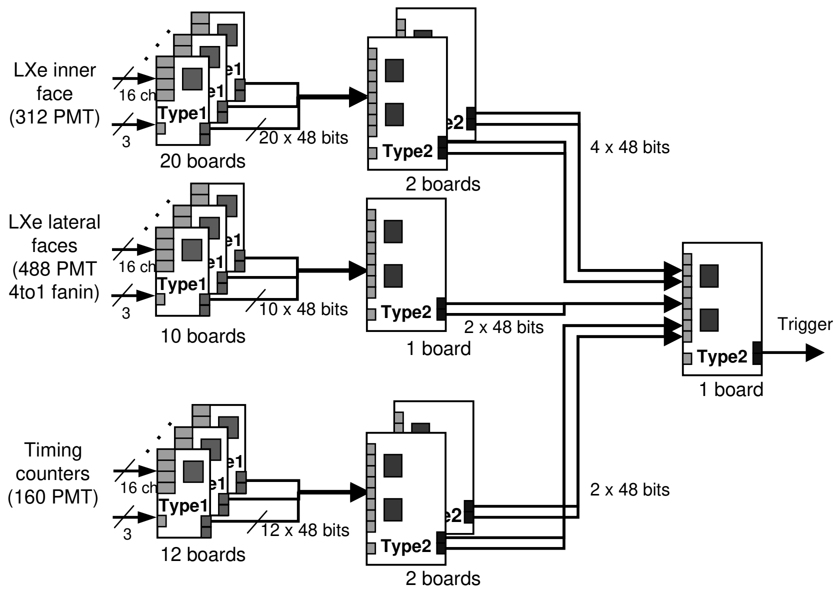

Figure 57: The trigger system structure: the 2 board types are used for the photon calorimeter and for the positron tracker. The boards are arranged in a tree structure.

in a tree structure, as shown in fig.57.

Board Type1 is a VME 6U circuit which accommodates 16 FADCs, while board Type2 is a VME 9U circuit with only digital inputs and outputs.

As indicated by the simulation, the front calorimeter face (entrance face) needs, for a good trigger performance, one FADC per PMT while for the lateral and outer faces a 4 PMT to one FADC fan-in should be tolerable. In this scheme the entire system can be arranged into 3 VME crates (two standard 6U and one 9U), for a total of 42 Type1 and 6 Type2 boards.

The clock frequency of the trigger system is 100 MHz . This choice is a satisfactory compromise between the cost and the availability of the components and the required performances. The system needs to be operated synchronously and for this reason the clock is distributed by means of Delay Locked Loop (DLL) components. The total trigger latency is evaluated to be 350 ns; this delay can easily be accommodated in the memory depth of the main waveform digitizer of the experiment.

9.3.5 Short description of the boards functions

Board Type1 contains 16 FADCs, one FPGA, a control section and 2 LVDS output connections, for a total throughput rate of 2×5 Gbits/s. The analog-to-digital conversion is performed with a 10 bit device with a 1 V dynamic range.

The Type1 boards have three distinct configurations accordingly to the sub-detector to which they are connected (see fig.57). The FPGA for the inner calorimeter face implements the following functions:

1. buffering of 16 PMT channels signals;
2. equalization of the PMT gains and, if needed, correction for PMT non linearity by means of Look Up Tables;
3. evaluation of each PMT baseline, and its subtraction from the corresponding signal;
4. search for the PMT corresponding to the maximum signal amplitude;
5. sum of the total collected charge;
6. definition of the signal timing with a precision of one fifth of the clock period;
7. control and debug capability of the data flow;

The boards configuration for the other calorimeter faces is similar to this but functions 4) and 6) are not required. The boards for the timing counter have a hit cluster finding algorithm that replaces functions 4) and 5).

Board Type2 contains 2 FPGAs, a control section, 10 input and 2 output LVDS connections, each one with a throughput rate of 5 Gbits/s. The 6 Type2 boards have 4 different FPGA configurations reflecting their different use in the trigger system. The algorithms that these FPGAs should implement are mainly a subset of those enumerated for board Type1. The chosen board size (VME 9U) is large enough to easily solve the signals routing on the printed circuit, without compromising the signals timing.

9.3.6 Trigger generation

The final board Type2 generate the trigger. The normal operation trigger rate has been evaluated to be $R_{L1} \approx 20$ Hz. The trigger system can generate also other triggers for debugging and calibration purposes. In particular a fraction of the triggers will be generated by relaxing a selection criteria at the time.

Furthermore external devices, like auxiliary calorimeters, may be included in the system for specific calibration purposes by simply adding a dedicated board Type1 in the structure. The redundant number of connections betwenn boards allows also the execution in parallel of different sets of trigger algorithms, without increasing the system complexity.

9.3.7 Present status

The FPGA configurations for board Type1 are designed and simulated, and all the requirements for the calorimeter board are met. The components selection for the first two prototype boards is terminated, and the components have been purchased. The printed circuit design of a prototype board is in progress. This prototype (Type0) is slightly different from a board Type1. It contains the 16 FADCs and the FPGA like board Type1, but it accommodates the control section of board Type2 and one input and one output LVDS. Two identical Type0 boards allow a complete system test including all critical aspects:

1. algorithms efficiency with real PMT signals ;
2. data transmission and reception among boards;
3. board synchronization;
4. trigger generation.

9.4 Data Acquisition Electronics

Pile-up in high rate experiments becomes a severe problem. The coincidence of a γ from radiative muon decay with two or three $\gamma's$ from positron anihilation can easily mimic a γ originating from a $\mu^+ \to e^+ + \gamma$ decay. While MC simulation have shown that two incident $\gamma's$ can be spatially separated if their conversion point is more than 15cm apart, an additional handle is needed. It has therefore been proposed to equip all PMTs with waveform digitizing in the multi-MHz range. Studies have shown that two γ rays, each with an energy greater than 2.5MeV, can be reconstructed if their time tifference is more than 10 nsec.

If the waveform digitizing could achive sampling speeds above 1GHz, its timing resolution would be better than 100ps using sample interpolation, and therefore the usage of conventional ADC's and TDC's could be avoided making the DAQ electronics much simpler. Flash ADC's in the GHz range are still too expensive to use on all 960 PMTs, but we can follow an earlier development made at PSI [23]. For a different experiment [24] an analog switched capacitor sampling chip has been designed. This chip consists of 128 capacitors, which sample the PMT input signal at a frequency of 500-1200 MHz. Instead of generating and distributing the sampling frequency directly, the capacitor switches are driven by an inverter chain, where a trigger signal propagates with high speed though a series of 128 double inverters. Since this is analog to a domino wave, the chip was named Domino Sampling Chip (DSC). When a waveform has been stored in the capacitors, they are read out at low speed (5 MHz) via a shift register and a commercial ADC (12 bit).

For the $\mu^+ \to e^+ + \gamma$ experiment, it has been concluded that a sampling speed of 2 GHz (500 ps bin width) is necessary to obtain a timing resolution of 50ps via bin interpolation, necessary for the positron timing counter and the

LXe calorimeter. If the domino wave runs in a circular fashion constantly and is only stopped by the trigger, the sampling capacitors can be used as an analog pipeline and delay cables can be avoided. This new chip, called Domino Ring Sampler (DRS) is currently designed at PSI. The number of storage capacitors has been increased to 1024 and the readout speed via the shift register to 40 MHz. Eight data channels and one calibration channel are integrated on a single chip, which is housed and read out by a custom VME board using 12 bit flash ADCs and FPGAs. The sampling depth of 512 ns accommodates a typical LXe scintillation pulse of 100ns width and a pipeline delay of 412 ns which is well above the expected level one trigger latency. A first prototype using a 0.25μ radiation hard technology has been submitted recently. Analog circuit simulations have shown that the domino wave runs stable at a speed of 2 GHz. The protoype will will be delivered to PSI in July 2002. After a second design iteration in fall 2002, it is expected to have a chip production run by early 2003 and a complete DAQ board ready be end of 2003.

The readout of all nine channels per chip with a single 40 MHz flash ADC consumes $230\mu s$, which is an acceptable dead time for an experiment running at $\sim$ 100Hz. After the readout, the waveform is processed in the onboard FPGAs. At a first step a baseline subtraction is applied in the same way as in the trigger boards. Then a zero suppression logic discards channels which have no hit to reduce the amount of readout data. The FPGA algorithm checks if a channel contains a single hit or if a pile-up occurred by calculating the first derivative and searching for zero crossings. In case of a pile-up, the full waveform is transferred to the backend computers for further analysis. If no pile-up occurred, the signal charge is calculated by numerical integration and the time is evaluated by fitting the leading edge. These two numbers are equivalent to traditional ADC and TDC values and sent to the backend computers instead of the full waveform which then reduces the amount of data dramatically.

While all photomultiplier signals will be digitized at 2GHz, the drift chamber signals are much slower and can be digitized directly with flash ADCs at 100MHz. Bin interpolation gives a timing resolution of $\sim$ 1-2nsec which is equivalent to a position resolution of 100μm. It is planned to use the trigger boards for drift chamber signal digitization since they contain all necessary hardware. The FPGA programming will be the same for the boards with the DRS chip and for the drift chamber DAQ boards.

Since the FPGAs are re-programmable through VME, the algorithm can be changed and optimized during the set-up of the experiment. If additional devices like scalers or constant fraction discriminators are necessary, they can be easily emulated in the FPGAs. It is planned to use VME boards with the DRS chip for the calorimeter readout and the trigger boards with 100 MHz digitizing for the readout of the anodes and cathodes of the drift chambers, thus eliminating the need of any other device except pre-amplifiers and waveform digitizers.

Waveform digitizing on all channels gives an excellent handle on pile-up and noise suppression. Using this technique, the noise level can be suppressed even further.

At a first stage in each FPGA, the baseline of a PMT or drift chamber signal is subtracted on an event-by-event basis. The baseline level is sampled before each pulse and averaged over several samples. This baseline value is then subtracted from the following pulse. This effectively removes any noise with frequencies below the signal width, including 50 Hz noise and its harmonics.

An alternative apprach, should it be necessary, is a complete frequency analysis of each signal. The power spectrum of the signal and the background is not flat over the whole frequency range. This leads to frequency bands where the signal-to-noise ratio is worse than in others. Most notable in the frequency ranges below 1kHz (50 Hz and its harmonics) and above 300MHz (digitization noise) show a very high background contribution. Thus by filtering the signal with a bandpass filter which attenuates these frequency bands, the overall signal-to-noise ratio can be improved. A detailed study about the possible level of supression will be made with signals from the completed detector showing a realistic noise pattern.

For sampling speeds in the GHz range, the pile-up rejection is not determined by the sampling speed but by the rise time of the signal. As a rule of thumb, two overlaying signals can be distinguished if they are separated by more than the risetime of the signal and they differ not more than a factor of ten in signal height. We measured a risetime of about 8ns for typical γ induced showers, which gives us a pile-up rejection of 10ns for individual channels, if the overlaying signals do not differ too much in height. For the pile-up of very small signals, the signal of several photomultipliers have to be combined and the shower shape has to be evaluated. It should be noted that this method reaches its limit if the overlayed signal becomes very small, like 511keV γ'r from positron anihilation. It therefore has to be made sure that this background is shielded sufficiently from the calorimeter.

Given the time resolving power of 10ns and spacial resolving power of 15cm, it has been reported already in the proposal (section 4.2.2), that the accidental photon pile-up rate is 5×10^{-15}.

9.5 DAQ Software

For the $\mu^+ \to e^+ + \gamma$ experiment we will use the MIDAS DAQ system [20], which has been sucessfully being used for many years in the PIBETA [24] experiment and has now become the standard DAQ system at PSI and TRIUMF. Besides all necessary means of data readout, transport and storage, MIDAS contains a full slow control system, an integrated data analysis functionality and a Web interface for remote control. While the curret version uses PAW for online data display and analysis, it is planned to switch to ROOT [25]. The software upgrade is scheduled for fall 2002 and supported with additional manpower from TRIUMF.

Automatic calibration and monitoring of the experiment can easily be integrated due to the close coupling of the main DAQ and the slow control. In the PIBETA experiment, the MIDAS analyzer evaluated all online energy spectra in regular intervals and adjusted the PMT high voltage if necessary. This ensured a long term stability of the experiment, which is planned to use in this experiment as well. An elaborate alarm system compares critical histograms with reference histograms and monitors important slow control variables such as xenon pressure and temperature. In case of problems, operators are notified by alarm sounds in the counting houase and by cellular phones.

Since the DAQ software framework is already existing, one can concentrate on the experiment specific code like shower reconstruction and particle tracking. While the first one is currently worked on by several collaboration members, the drift chamber tracking will be taken care of by a newly hired person at PSI in fall 2002.

The expected data rate depends on the trigger rate and the waveform compression in the front end electronics. In addition to $\mu^+ \to e^+ + \gamma$ triggers, we will have a mixture of other triggers for calibration and background analysis. Assuming an overall trigger rate of 100Hz and an average channel occupancy of 50% for the calorimeter and 10% for the drift chamber and positron counter, the waveform data amounts to 1.2MB/event or 120MB/sec. To process this data, a online linux cluster is planned where each node processes a manageable data stream of less than 10MB/sec. Since we want to keep all waveforms for potential $\mu^+ \to e^+ + \gamma$ events but not for the calibration events, a third level trigger will be implemented in this computer farm. For events which are not close to $\mu^+ \to e^+ + \gamma$ events, the waveforms will be analyzed online and only ADC and TDC data will be stored, reducing the data amount dramatically to about 10kB per event. For the other events the waveforms can be compressed in the linux farm. The experience of the PIBETA experiment has shown that typical compression rates of a factor of ten are possible. If we decide to keep waveforms for events at a 10Hz rate and only ADC and TDC values for the other 90Hz, the data rate becomes 10 x 1.2MB x 0.1 + 90 x 0.01MB = 2.1MB per second which can be taped easily using current DLT technology.

References

[1] "Search for $\mu^+ \to e^+ + \gamma$ down to 10^{-14} branching ratio," PSI Proposal R-99.05.1, May 1999.

[2] MEGA Collaboration, "Search for the lepton-family-number non-conserving decay $\mu^+ \to e^+\gamma$," hep-ex/0111030.

[3] MECO Collaboration, "A Search for $\mu^- N \to e^- N$ with Sensitivity below 10^{-16}," AGS proposal P940, 1997.
http://meco.ps.uci.edu/

[4] Update & Supplement to LOI R-98-05.0/1, BV29, July 1999.

[5] "Report on the Progress for the $\mu^+ \to e^+\gamma$ Experiment at PSI", Progress Report Jan. 2002.

[6] Detector Description and Simulation Tool, Applications Software Group CERN, CERN Program Library Writeup W5013 (1993).

[7] TRANSPORT- A Computer Program for Designing Charged Particle Beam Transport Systems, K.L. Brown *etal*. CERN Yellow Report 73-16, (1973); Decay TURTLE- A Computer Program for Simulating Charged Particle Beam Transport Systems, including Decay Calculations, K.L. Brown and Ch. Iselin, CERN Yellow Report 74-2 (1974);
Graphics versions of both Programmes by U. Rohrer PSI-Report (1980).

[8] muegamma technical note TN015, June 2002.
(http://meg.psi.ch/doc/index.html)

[9] "R&D Report on the drift chamber prototype at Univ. of Tokyo",May 2001, Muegamma technical note TN013.
(http://meg.psi.ch/doc/index.html)

[10] "Report on the Progress for the $\mu^+ \to e^+\gamma$ Experiment at PSI", Progress Report, January 2001.

[11] K. Abe *et al.*, MEG-TN012 (2000).

[12] MUEGAMMA Collaboration, PSI Annual Report (2001).

[13] R. Bellazzini *et al.*, Nucl. Instr. and Meth. **A 457** (2001) 22.

[14] H. Kichimi *et al.*, Nucl. Instr. and Meth. **A 453** (2000) 315.

[15] muegamma technical note TN017, June 2002.
(http://meg.psi.ch/doc/index.html)

[16] muegamma technical note TN014, Apr. 2002.
(http://meg.psi.ch/doc/index.html)

[17] N.Ishida *et al.*, Nucl. Instr. and Meth. **A834** (1997) 380-386.

[18] G. M. Seidel, R. E. Lanou and W. Yao, "Rayleigh scattering in rare-gas liquids" hep-ex/0111054

[19] S.Belforte *et al.*, SVT Technical Design Report, CDF note 3108 (1994); CERN EP report 81-12/ReV.

[20] MIDAS home page, http://midas.psi.ch

[21] http://products.analog.com/products/info.asp?product=AduC812

[22] http://www.cygnal.com/products/C8051F000.htm

[23] C. Brönnimann *et al.*, Nucl. Instr. and Meth. **A 420**, 264 (1999)

[24] PIBETA experiment at PSI, http://pibeta.psi.ch

[25] http://root.cern.ch